UNIVERSITY OF OKLAHOMA

GRADUATE COLLEGE

NUMERICAL SIMULATION OF THE EFFECTS OF RESERVOIR

HETEROGENEITY, FRACTURES, AND MULTI-WELL INTERFERENCE

ON PRESSURE TRANSIENT RESPONSES

USING MULTISTENCILS FAST MARCHING METHOD

A THESIS

SUBMITTED TO THE GRADUATE FACULTY

in partial fulfillment of the requirements for the

Degree of

MASTER OF SCIENCE

By

SANGCHEOL YOON
Norman, Oklahoma
2017

NUMERICAL SIMULATION OF THE EFFECTS OF RESERVOIR
HETEROGENEITY, FRACTURES, AND MULTI-WELL INTERFERENCE
ON PRESSURE TRANSIENT RESPONSES
USING MULTISTENCILS FAST MARCHING METHOD

A THESIS APPROVED FOR THE
MEWBOURNE SCHOOL OF PETROLEUM AND GEOLOGICAL ENGINEERING

BY

_____
Dr. Siddharth Misra, Chair

_____
Dr. Deepak Devegowda

_____
Dr. Zulfiquar Reza

This thesis is dedicated to my parents and my brother.

ACKNOWLEDGEMENTS

TABLE OF CONTENTS

LIST OF TABLES

LIST OF FIGURES

ABSTRACT

Analysis of rate and pressure transient responses of a well in spatially heterogeneous reservoir cannot be performed using conventional well-test analytical equations. An accurate analysis of transient pressure/rate responses of wells in heterogeneous naturally fractured reservoirs requires precise characterization of the complex interactions between various reservoir and well features. These features include heterogeneity, natural and induced fractures, reservoir boundaries, and well interference. Single-stencil fast marching (SFM) method has been used for pressure transient analysis (PTA) and history matching in heterogenous reservoirs. As an improvement to the SFM method, we develop and test the multistencils fast marching (MFM) method, which exhibits one order of magnitude higher accuracy compared to SFM method. We extensively validate the MFM method for various reservoir and wellbore scenarios by comparing its predictions against those of SFM Method, KAPPA Saphir analytical model, and KAPPA Rubis numerical model. MFM method can be effectively used to estimate pressure response not only in homogeneous reservoir with heteromorphous geometry of no-flow boundary but also in highly heterogeneous reservoir affected by high contrast permeability/porosity distribution and in the presence of induced/natural fractures or impermeable zones. Furthermore, using embedded fracture multistencils fast marching (EFMFM) method, we improve MFM method to model a discrete fracture on the cartesian reservoir girds. Through EFMFM method, pressure response data can be estimated accurately not only in a computationally efficient way, but also in an intuitive way with the visualization of the time-varying drainage volume.

CHAPTER 1: INTRODUCTION

1.1 Background

Numerical simulation of pressure propagation is widely used in unconventional reservoir characterization to understand the effects and interaction of spatial heterogeneity and complex fracture geometries and distributions. Such a simulation is required for accurate prediction of reservoir performance. Numerical simulation is time-consuming owing to the need of high-resolution grid refinement to account for reservoir heterogeneity and complex geometries. Pressure/rate transient responses of a well can be analyzed using well-test analytical equations and numerical reservoir flow simulators to estimate reserves, production forecasting, and diagnostics of hydraulic fracturing. Most well-test analytical equations are derived for homogenous reservoirs and are limited in their adaptability to heterogeneous reservoirs. A fundamental concept involved in pressure/rate transient analysis in homogeneous reservoir is the radius of investigation (ROI). Time-varying location of the maximum rate of pressure change produced due to the propagation of pressure pulse from a point source (well) into the reservoir away from the wellbore is defined as the ROI. The radius of pressure pulse propagation can be estimated by solving Eikonal equation which describes motion of wave front propagation. The way to characterize the geometry of a front expending outwards is to compute the travelling time in which the front reaches each coordinate over the medium. Fast marching (FM) method is a case of level set methods and a powerful solution for the Eikonal equation. It is composed of a computationally efficient algorithm for tracking the propagation of a physical wave front. Though the fast marching method has limitations that extension to higher number of dimensions needs expensive cost in

computational time and it requires extensive evaluation for discretized space, it has been developed and applied into various research fields including image segmentation, motion planning in robotics, path planning for intelligent navigation of an unmanned surface vehicle, etc. (Dirami et al., 2012, Janson et al., 2015, Liu et al., 2017). Fast marching method can also efficiently track the pressure front propagation and ROI in heterogeneous reservoirs with complex fracture systems. Computational complexity of this method lies in between those of numerical simulators and analytic solutions. In this thesis, we develop the MFM method and test its accuracy against analytical solutions, numerical solutions, and SFM predictions in various reservoir scenarios such as homogeneous reservoirs, fractured reservoirs, and reservoirs with heterogeneous permeability distribution. In addition, we propose a new method, named embedded fracture MFM method (EFMFM) for fracture modeling.

CHAPTER 2: METHODOLOGY FOR TRACKING PRESSURE FRONT USING MULTISTENCILS FAST MARCHING

This chapter presents the steps involved in the transformation of the Diffusivity equation to the pressure solution for a fixed rate draw-down using MFM method which can solve the Eikonal equation representing the high-frequency (asymptotic) solution of the diffusivity equation for a pressure impulse at the well. High-frequency limit represents most rapidly varying portion of the solution that corresponds to the propagation front.

2.1 Asymptotic Solution for Diffusivity Equation

Diffusivity equation can be solved to obtain pressure transients within a porous medium exhibiting heterogeneous permeability distribution. Diffusivity equation is expressed as

$$\phi(x)\mu c_t \frac{\partial p(x,t)}{\partial t} = \nabla \cdot \{k(x) \cdot \nabla p(x,t)\} \tag{2.1}$$

where vector x denotes a point in the reservoir, scalars $k(x)$ and $\phi(x)$ denote the permeability and porosity of the reservoir, respectively, at the location x. Those two properties depend on geometric configuration of medium and time along with liquid flow assumption that compressibility, c_t, and fluid viscosity, μ, are constant in isotropic and fully saturated formation. Equation 2.1 is converted to frequency domain using Fourier transform.

$$\phi(x)\mu c_t(-i\omega) \frac{\partial \tilde{p}(x,\omega)}{\partial \omega} = k(x) \cdot \Delta\tilde{p}(x,\omega) + \nabla k(\mathrm{x}) \cdot \nabla\tilde{p}(x,\omega) \tag{2.2}$$

Frequency domain solution of Equation 2.2 is given as (Fatemi et al., 1995)

$$\tilde{p}(x, \omega) = e^{-\sqrt{-i\omega}\tau(x)} \sum_{n=0}^{\infty} \frac{A_n(x)}{(\sqrt{-i\omega})^n}, \tag{2.3}$$

where $A_n(x)$ is the amplitude of the nth order pressure wave at point x. The first 0th order term $A_0(x)$ represents the high-frequency limit. Consequently, the high-frequency solution of Equation 2.1 in the frequency domain is expressed as

$$\tilde{p}(x, \omega) = e^{-\sqrt{-i\omega}\tau(x)} A_0(x) \tag{2.4}$$

Upon performing the inverse Fourier transform on Equation 2.4, following 2D time-domain solution is obtained:

$$p(x, t) = \frac{\tau(x)}{2\sqrt{\pi t}} e^{\frac{\tau(x)^2}{4t}} A_0(x) \tag{2.5}$$

Considering the highest order term of $\sqrt{-i\omega}$, i.e. $(\sqrt{-i\omega})^2$, when Equation 2.4 is substituted into Equation 2.2, we obtain the Eikonal equation representing the high-frequency (asymptotic) solution of the diffusivity equation for a pressure impulse, expressed as

$$\nabla\tau \cdot \nabla\tau = \frac{\phi(x)\mu c_t}{k(x)} = \frac{1}{\alpha}$$

$$|\nabla\tau|\sqrt{\alpha} = 1, \tag{2.6}$$

Therefore, Eikonal equation quantifies the propagation of the pressure front or the time-varying drainage area (Vasco et al., 2000). Pressure front is defined as the maximum pressure response in the reservoir for an impulse source in the well (King et al., 2016). The high-frequency solution is associated with the arrival time of the peak slope of the pressure transient that is governed by the reservoir properties. The equation

governing the diffusive time of flight (DTF) related to the pressure front propagation process can be expressed as

$$|\nabla\tau(\mathbf{x})|\sqrt{\frac{k(\mathbf{x})}{\phi(\mathbf{x})\mu c_t}} = 1 \tag{2.7}$$

The entire term inside the square root is referred as the diffusivity α. The time-varying DTF is also denoted as $\tau(x)$ for the point x and has the unit of time 0.5. This approach is similar to the solution for the location of propagating wave front in wave theory. Equation 2.7 indicates that DTF is inversely dependent on square root of diffusivity α. Here, it is assumed that the pressure depends only on the DTF, which is equivalent to an assumption that the contour lines of pressure are strongly related to the contour lines denoting the DTF (King et al., 2016), who assumed $p(x,t) \approx p(\tau(x),t)$ to reduce 3D diffusivity equation to equivalent 1-D form. Datta Gupta et al. (2011) used this concept to find the ROI as a function of time in pressure transient analysis. Multistencils fast marching (MFM) method is implemented to solve the Eikonal equation to assess the DTF, which can be used to derive the pressure propagation in a heterogeneous reservoir.

2.2 Multistencils Fast Marching Method (MFM)

Fast marching (FM) method is class of solutions designed to solve the Eikonal equation to aid in the determination of position of the pressure front. This method is based on the observation that arrival time of the pressure front at any node is only dependent on the smallest value of arrival time among the immediate neighboring nodes, which is referred as the "causality relationship" and is the basis of fast marching methods (Sethian, 1996). Several improved FM methods, such as Higher Accuracy Fast Marching method,

Shifted Grid Fast Marching Method, Untidy Fast Marching method, and Multistencils Fast Marching (MFM) method, have been proposed to enhance the accuracy of FM predictions. Most FM algorithms, except MFM algorithm, ignore information of nodes in the diagonal direction while considering only the 4-adjacent neighboring nodes in the 2D plane; consequently, having larger prediction errors along the diagonal directions. The MFM method eliminates this limitation by utilizing information from all neighboring nodes. In this paper, the accuracy of the MFM method is further improved by numerically approximating the gradient in the Eikonal equation as a second-order finite difference formulation whenever the arrival times of the neighbor points are available, which is also implemented in the development of the Higher Accuracy Fast Marching method (Hassouna and Farag, 2007). By combining the concepts of MFM method and HAFM method, we develop and apply second-order MFM method in this thesis for modeling pressure propagation in a heterogeneous reservoir. The step-wise explanation of the second-order MFM approach is described in **Figure 2.1.** The first node is selected (black circle, **Figure 2.1a**) at the impulse source and DTF at the first node is assigned $\tau = 0$ at r $= r_w$. DTF is then calculated for the 8 neighboring nodes (light gray circles, **Figure 2.1b**) surrounding the first node in the 2D plane. Out of the 8 DTFs calculated for the neighboring nodes, the node with minimum value of DTF is selected and 'accepted' (dark gray circle, **Figure 2.1b**). Following that, the stencil is moved to the neighboring newly accepted node and the DTF is calculated for the 10 neighboring nodes   surrounding the first node and the next selected node (light gray circles, **Figure 2.1c**). The stencil is moved to the neighboring newly accepted node and the DTF is calculated for the 3 extra neighboring nodes surrounding the newly accepted node. The DTF is compared for all

6

the 10 neighboring nodes (light gray circles, **Figure 2.1c**) including previously calculated

DTF from the first node to select the next node with minimum value of DTF. This process

is repeated through all the nodes in the reservoir domain till the DTFs for all points are

determined (**Figure 2.1d**, **Figure 2.1e**). The key difference between multistencils and

single-stencil approach is the number of neighboring nodes considered at each time-step.

(a)   (b)   (c)   (d)   (e)
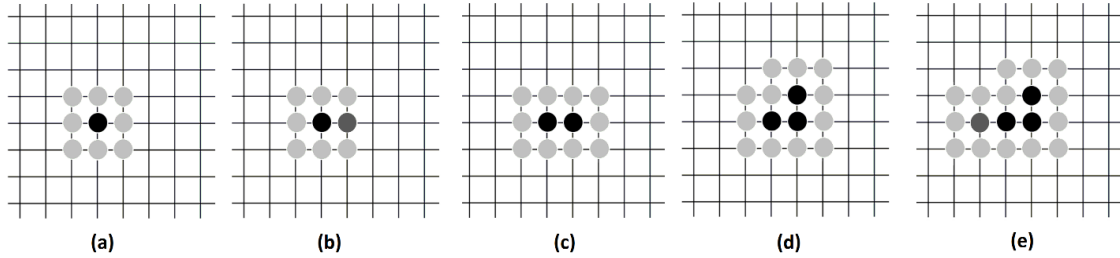
Figure 0.1: Algorithm of multistencils fast marching (MFM) method

2.3 Drainage Volume and Pressure Transient Analysis

MFM algorithm tracks the temporal and spatial evolution of the drainage volume.

In order to formulate the drainage volume as a function of physical time, τ calculated

using the MFM approach needs to be transformed to the physical time t. The relationship

used in this thesis is $\tau^2 = 4t$, which is based on the assumption that pressure depletion will

not occur beyond the pressure front during a 2-D radial flow; therefore, the flow can be

considered as a pseudo steady state flow with a transient reservoir boundary. Finally, a

geometric approximation of the drainage volume is used to relate the well rates with the

pressure response of a well. Multistencils fast marching (MFM) method solves Eikonal

equation, derived in section 2.1, to compute Diffusivity Time of Flight (DTF) at all the

nodes. Following that, diffusivity equation in three dimensions is transformed to one

dimensional space formed using DTF as the new spatial coordinate (Zhang et al., 2015).

In doing so, the drainage volume can be related to DTF. Diffusivity equation is expressed

as

$$\phi c_t \frac{\partial p}{\partial t} = \nabla \cdot \{\phi c_t \alpha \nabla p\} \qquad (2.8)$$

High-frequency solution of Diffusivity equation generates the Eikonal equation expressed as

$$|\nabla \tau| = \frac{1}{\sqrt{\alpha}} \qquad (2.9)$$

In order to perform the dimensional transformation of Diffusivity equation from radial coordinates to DTF coordinates, a strong relationship is assumed between pressure contours and DTF contours, such that $p(x,t) \approx p(\tau(x), t)$. In other words, pressure gradient direction aligns with the DTF gradient direction (Zhang et al., 2015). Pressure gradient with respect to DTF can then be written as

$$\nabla p = \frac{\partial p}{\partial \tau} \nabla \tau \qquad (2.10)$$

Equation 2.9 when incorporated into Equation 2.10 generates

$$\nabla p = \frac{\partial p}{\partial \tau} \frac{1}{\sqrt{\alpha}} \mathbf{n}_\tau \qquad (2.11)$$

where $\mathbf{n}_\tau$ is the inward-pointing unit normal vector to the contour of τ. Substituting Equation 2.11 into Equation 2.8, we get

$$\phi c_t \frac{\partial p}{\partial t} = \nabla \cdot \left(\phi c_t \sqrt{\alpha} \frac{\partial p}{\partial \tau} \mathbf{n}_\tau \right) \qquad (2.12)$$

To work with Equation 2.12, divergence operator needs to be applied on $\mathbf{n}_\tau$ that requires coordinate transformation from Cartesian coordinate system to ($\boldsymbol{\tau}$, $\boldsymbol{\psi}$, $\boldsymbol{\kappa}$), such that $\boldsymbol{\tau}$ is the direction of the DTF and the other two coordinates, $\boldsymbol{\psi}$ and $\boldsymbol{\kappa}$ are orthogonal directions to each other and to $\boldsymbol{\tau}$. Thus, the divergence of vector $\mathbf{n}_\tau$ in the direction of τ can be expressed as

$$\nabla \cdot \mathbf{n}_\tau = \frac{1}{h_\tau h_\psi h_\kappa} \left[\frac{\partial (h_\psi h_\kappa n_\tau)}{\partial \tau} \right] \tag{2.13}$$

where h_τ, h_ψ, and h_κ are the lengths of the covariant vectors. On applying the divergence

operator, Equation 2.12 converts to

$$\phi c_t \frac{\partial p}{\partial t} = \frac{1}{h_\tau h_\psi h_\kappa} \frac{\partial}{\partial \tau} \left(\phi c_t h_\psi h_\kappa \sqrt{\alpha} \frac{\partial p}{\partial \tau} \right) \tag{2.14}$$

According to the definition of covariant vector, h_τ is equal to $\sqrt{\alpha}$. Also, the

product $h_\tau h_\psi h_\kappa$ is simply the Jacobian J of the coordinate transformation. Therefore,

Equation 2.14 reduces to

$$J\phi \frac{\partial p}{\partial t} = \frac{\partial}{\partial \tau} \left(J\phi \frac{\partial p}{\partial \tau} \right) \tag{2.15}$$

J and ϕ are functions of (τ, ψ, κ) in general. Double integral of Equation 2.15

over the coordinates ψ and κ generates

$$\omega(\tau) \frac{\partial p}{\partial t} = \frac{\partial}{\partial \tau} \left[\omega(\tau) \frac{\partial p}{\partial \tau} \right] \tag{2.16}$$

where

$$\omega(\tau) = \iint \phi J(\tau, \psi, \kappa) \, d\psi d\kappa \tag{2.17}$$

Drainage pore volume in the (τ, ψ, κ) coordination system is expressed as

$$V_p(\tau) = \iiint \phi J(\tau, \psi, \kappa) \, d\tau d\psi d\kappa \tag{2.18}$$

Consequently, $\omega(\tau)$ can be reformulated as

$$\omega(\tau) = \iint \phi J(\tau, \psi, \kappa) \, d\psi d\kappa = \frac{\partial V_p(\tau)}{\partial \tau} \tag{2.19}$$

Equation 2.16 can be simplified using Equation 2.19 as

$$\frac{\partial V_p(\tau)}{\partial \tau}\frac{\partial p(\tau,t)}{\partial t} = \frac{\partial}{\partial \tau}\left(\frac{\partial V_p(\tau)}{\partial \tau}\frac{\partial p(\tau,t)}{\partial \tau}\right) \tag{2.20}$$

This is the 1D Eikonal equation in terms of the DTF.
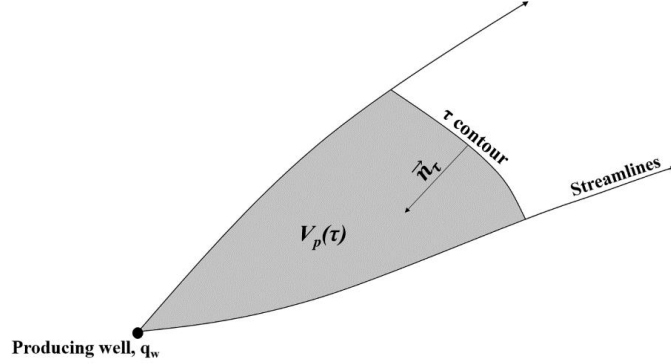
Figure 0.2: A cartoon of streamlines and DTF contour (adapted from King et al., 2016)

In **Figure 2.2**, the flux is chosen inwards pointing to the well to accommodate positive flux for a producing well. The volume between streamlines and the DTF contour is the time-varying drainage pore volume (V_p). At any location x, the rate of change in the drainage pore volume is the porosity at that location. The inward-pointing normal vector ($\mathbf{n}_\tau$) to the propagation of pressure front is related to the negative gradient of the drainage volume (V_p). Based on the above two statements and Equation 2.19, we can formulate the following

$$A\phi\mathbf{n}_\tau = -\nabla V_p(\tau) = -\omega(\tau)\nabla\tau \tag{2.21}$$

Using Equations 2.21 and 2.9, flow rate (flux) in Cartesian coordinates can be transformed to the (τ, ψ, κ) coordinates as follows

$$q(\tau,t) = -\frac{kA}{\mu}\mathbf{n}_\tau \cdot \nabla p = -\frac{kA}{\mu}\mathbf{n}_\tau \cdot \left[\nabla\tau\frac{\partial p}{\partial \tau} + \nabla\psi\frac{\partial p}{\partial \psi} + \nabla\kappa\frac{\partial p}{\partial \kappa}\right]$$

$$\approx \frac{kA}{\mu}\frac{\omega(\tau)\nabla\tau}{A\phi}\cdot\frac{\partial p}{\partial \tau}\nabla\tau = c_t\omega(\tau)\frac{\partial p}{\partial \tau} \tag{2.22}$$

Using Equation 2.22, the diffusivity equation expressed as 2.20 can be restated in terms of the flux in 1D as

$$c_t \frac{\partial p(\tau, t)}{\partial t} = \frac{\partial q(\tau, t)}{\partial V_p(\tau)} \tag{2.23}$$

Integrability of pressure requires (King et al., 2016)

$$\frac{\partial}{\partial \tau} \frac{\partial p(\tau, t)}{\partial t} = \frac{\partial}{\partial t} \frac{\partial p(\tau, t)}{\partial \tau} \tag{2.24}$$

Equation 2.24 facilitates the derivation of 1D Diffusivity equation in terms of flux expressed as

$$\frac{\partial q(\tau, t)}{\partial t} - \frac{\partial V_p(\tau)}{\partial \tau} \frac{\partial}{\partial \tau} \left(\frac{\partial \tau}{\partial V_p(\tau)} \frac{\partial q(\tau, t)}{\partial \tau} \right) = 0 \tag{2.25}$$

Dimensionless Boltzmann ratio ξ is expressed in terms of τ and t as

$$\xi = \frac{\tau^2}{4t} \tag{2.26}$$

Using this dimensionless variable, derivatives of the flow rate are expressed as

$$\frac{\partial q(\tau, t)}{\partial \tau} = \frac{\tau}{2t} \frac{dq(\tau, t)}{d\xi} \quad \text{and} \quad \frac{\partial q(\tau, t)}{\partial t} = -\frac{\tau^2}{4t^2} \frac{dq(\tau, t)}{d\xi} \tag{2.27}$$

Therefore,

$$\frac{\partial q(\tau, t)}{\partial t} = -\frac{\tau^2}{4t^2} \frac{2t}{\tau} \frac{\partial q(\tau, t)}{\partial \tau} = -\frac{\tau}{2t} \frac{\partial q(\tau, t)}{\partial \tau} \tag{2.28}$$

Using Equation 2.25 and 2.27, Equation 2.23 can be transformed to

$$\frac{\tau}{2t} \left(\frac{1}{w(\tau)} \frac{\partial q(\tau, t)}{\partial \tau} \right) + \frac{\partial}{\partial \tau} \left(\frac{1}{w(\tau)} \frac{\partial q(\tau, t)}{\partial \tau} \right) = 0 \tag{2.29}$$

11

In this form, the diffusivity equation may be integrated explicitly with the initial and boundary conditions. It requires one initial condition and two boundary conditions. For a fixed flow rate drawdown in an infinite domain, the initial and boundary conditions are (King et al., 2016):

$$t = 0: \qquad p = p_i \qquad q = 0$$

$$\tau = 0: \qquad\qquad q = q_w$$

$$\tau \to \infty: \qquad p \to p_i \qquad q \to 0$$

and the solution is obtained by solving the restated Equation 2.29 in the form of

$$\frac{\frac{\partial}{\partial \tau}\left(\frac{1}{w(\tau)}\frac{\partial q(\tau, t)}{\partial \tau}\right)}{\left(\frac{1}{w(\tau)}\frac{\partial q(\tau, t)}{\partial \tau}\right)} = -\frac{\tau}{2t} \tag{2.30}$$

Integrating the Equation 2.30 within an arbitrary function of time in terms of DTF leads to

$$\int_0^\tau \frac{\frac{\partial}{\partial \tau}\left(\frac{1}{w(\tau)}\frac{\partial q(\tau, t)}{\partial \tau}\right)}{\left(\frac{1}{w(\tau)}\frac{\partial q(\tau, t)}{\partial \tau}\right)}d\tau = \int_{\tau=0}^\tau -\frac{\tau}{2t}d\tau$$

$$\left[\ln\left(\frac{\partial \tau}{\partial V_p(\tau)}\frac{\partial q(\tau, t)}{\partial \tau}\right)\right]_0^\tau = -\frac{\tau^2}{4t}$$

$$\ln\left(\frac{\partial \tau}{\partial V_p(\tau)}\frac{\partial q(\tau, t)}{\partial \tau}\right) - \ln\frac{q(0, t)}{V_p(0, t)} = -\frac{\tau^2}{4t} \tag{2.31}$$

With the IC and BC conditions mentioned above, we end up with

12

$$\frac{\partial \tau}{\partial V_p(\tau)} \frac{\partial q(\tau, t)}{\partial \tau} = -\frac{q_w}{V_p(t)} e^{-\frac{\tau^2}{4t}} \tag{2.32}$$

Using Equation 2.24, the asymptotic solution to the diffusivity equation for a fixed rate draw-down in an infinite domain is expressed as

$$c_t \frac{\partial p(\tau, t)}{\partial t} = \frac{1}{w(\tau)} \frac{\partial q(\tau, t)}{\partial \tau} = -\frac{q_w}{V_p(t)} e^{-\frac{\tau^2}{4t}} \tag{2.33}$$

Now, we need to know a relationship between the physical time t and the diffusive time of flight τ to find the pressure in the reservoir. During the propagation of pressure in the heterogeneous reservoir, we describe the characteristic of pressure drop as pseudo steady state with an assumption of no-flow at the edges of pressure front. Therefore, the exponential terms tend to 1. Using this relationship, we can integrate the equation with time to determine the pressure drop after the drainage volume is calculated using the MFM method. The solution for a fixed rate draw-down is written as

$$\Delta p(\tau, t) = \frac{q_w}{c_t} \int_{t=0} \frac{dt}{V_p(t)} e^{-\frac{\tau^2}{4t}} \approx \frac{q_w}{c_t} \int_{t=0} \frac{dt}{V_p(t)} \tag{2.34}$$

For a fixed rate draw-down in an infinite domain, we have:

$$\Delta p(\tau, t) = \frac{q_w}{c_t} \int_{t=0} \frac{dt}{V_p(t)} e^{-\frac{\tau^2}{4t}} \tag{2.35}$$

Bourdet-type derivative of pressure in wellbore can then be expressed as

$$p'_{wf} = \frac{d\Delta p_{wf}}{d\ln(t)} = t \frac{d\Delta p(\tau, t)}{dt} \bigg|_{\tau=0} = \frac{q_w t}{c_t V_p(t)} \tag{2.36}$$

CHAPTER 3: VALIDATIONS OF MFM-BASED PRESSURE FRONT SIMULATION

3.1 Accuracy of MFM method

Several numerical experiments are performed to test the accuracy of the proposed second-order MFM method for two-dimensional front tracking applications. These experiments are necessitated because of the limited literature on validations of FM predictions of pressure front propagation. First, MFM and SFM predictions of travel time are compared against an assumed analytical solution. Second, MFM predictions are compared against those of SFM method in terms of radius of investigation in a reservoir with homogeneous and heterogeneous permeability distribution. Further, predictions of the proposed MFM method are compared those of previously published models. Finally, commercial KAPPA Rubis numerical and KAPPA Saphir analytical models are used for the numerical validation of MFM predictions in complex reservoir scenarios, such as vertical fractured well in naturally fractured reservoir. All the numerical experiments assume a centrally located single vertical well producing at a constant flow rate.

3.1.1 Multistencils Fast Marching vs. Single-stencil Fast Marching vs. Analytic Models

Similar to Hassouna and Farag (2007), we compare the error norms for SFM and the proposed second-order MFM predictions of travel-time isocontour lines in 2D plane against an assumed analytical travel-time function (**Figure 3.1a**). Discrepancies between the computed travel time $T(x)$ obtained using MFM and SFM methods and the assumed analytical travel-time solution $T_a(x)$ at any given node on the 2D plane located at x are quantified using the following three error norms:

$$L_1 = \frac{1}{n} \sum_{i=1}^{n} |T - T_a| \tag{3.1}$$

$$L_2 = \frac{1}{n} \sum_{i=1}^{n} |T - T_a|^2 \tag{3.2}$$

$$L_\infty = \max(|T - T_a|) \tag{3.3}$$

Where n is the total number of nodes defined on the 2D planar reservoir for modeling purposes.

In **Figure 3.1**, a large rectangular reservoir with a distinct distribution of diffusivity is modeled as a 2D plane with uniformly placed 101 nodes by 101 nodes. The reservoir model has 1 centrally located node identifying the well location (the source of pressure), 400 nodes at the edges identifying the reservoir boundary, and 9800 nodes identifying the reservoir nodes located inside the reservoir boundary. Analytical travel-time function assumed for this numerical experiment is $T_a(x) = \sqrt{(x - x_0)^2 + (y - y_0)^2} - 1$. In doing so, we invoke Equation 2.7 to obtain the reservoir diffusivity at all nodes as a continuously differentiable function (**Figure 3.1a**), which can be assumed as a permeability distribution if other parameters in the diffusivity term α are assumed to be constant. Following that, SFM and MFM methods are implemented to model the 2D pressure front propagation in the large reservoir with the aforementioned distribution of diffusivities. Various error norms for this comparison are listed in **Table 3.1**, which includes 1st and 2nd order SFM and MFM predictions. Error norms in **Table 3.1** illustrate that second-order MFM method enhances the accuracy by almost an order of magnitude compared to the other methods.
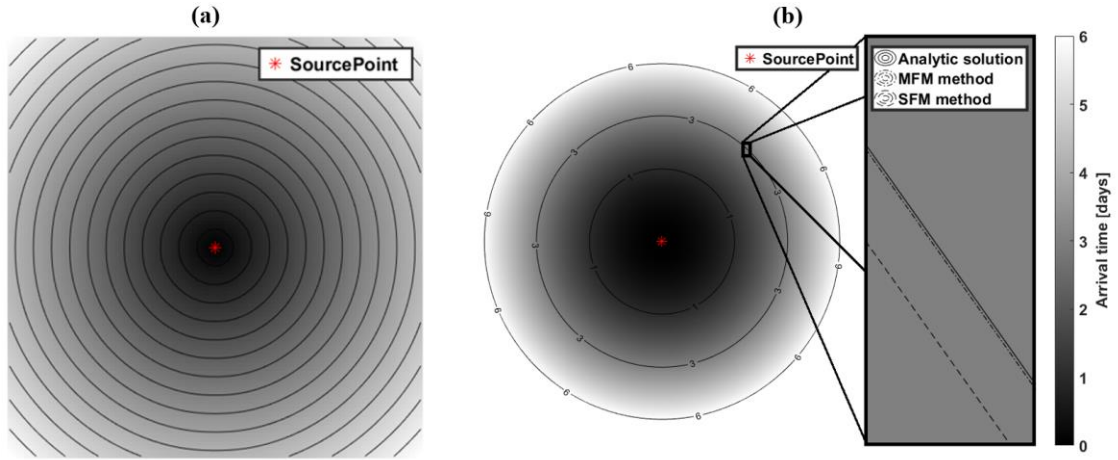
Figure 0.1: (a) Distribution of diffusivity in a large square-shaped reservoir for comparing the error norms of SFM and MFM travel-time predictions against an assumed analytical travel-time function, and (b) radius of investigation (ROI) contour lines generated using SFM and MFM methods along with those calculated using exact solution of ROI in a large homogenous reservoir spread across a 20,000 ft by 20,000 ft square-shaped area.

Table 3.1: Error norms of computed travel time $T(x)$ for various fast marching methods.

	Error norms		
	L_1	L_2	L_∞
1st order SFM	0.74610	0.69709	1.31485
2nd order SFM	0.19740	0.04234	0.32895
1st order MFM	0.60693	0.44561	0.97252
2nd order MFM	0.03961	0.00250	0.18765

Figure 3.1b compares the radius of investigation predicted using SFM and MFM

methods against that derived using the well-established analytic solution. The

comparison is performed for a large square-shaped homogeneous reservoir spread across

20,000-ft by 20,000-ft with an impulse pressure source in the centrally located well. The

reservoir and fluid properties assumed for this comparison are listed in **Table 3.2**. As the

pressure front propagates farther in the reservoir, the differences between predictions of each method and analytic solution decreases (**Table 3.3**). At 25th hour, the relative errors in SFM prediction is 0.5% and that in MFM prediction is 0.05%, which decreases to 0.1% and 0.01%, respectively, at the 75th hour. At both the times, the accuracy of MFM is one order higher than that of SFM. In **Figure 3.1b**, the accuracy of MFM method in comparison to SFM method is visually demonstrated using isocontour lines.

Table 3.2: Properties assumed for the case involving a vertical well centrally located in a large square-shaped homogeneous reservoir spread across 20,000-ft by 20,000-ft.

Reservoir property	
Dimension	*20,000 ft X 20,000 ft*
Grid size	*10 ft X 10 ft*
Matrix permeability	*100 md*
Porosity	*0.20*
Fluid property	
Viscosity	*1 cp*
Total compressibility	*$1.0 X 10^{-6} psi^{-1}$*

Table 3.3: Radius of investigation computed using various methods for the case involving a vertical well centrally located in a large square-shaped homogeneous reservoir spread across 20,000-ft by 20,000-ft.

	Radius of Investigation		
	Analytic	SFM	MFM
25 hours	*3631 ft*	*3600 ft*	*3628 ft*
75 hours	*6290 ft*	*6280 ft*	*6289 ft*

In heterogeneous reservoirs with smoothly varying permeability distribution (**Figure 3.2a**), the difference in accuracies of SFM and MFM method predictions for pressure propagation from a centrally located well is noticeable in terms of the predicted isocontour lines showing the edges of pressure front propagation (**Figure 3.2b**) and time-varying drainage volume (**Figure 3.3**). The reservoir, well, and fluid properties assumed for this comparison are listed in **Table 3.4**. At the 10th day, there is a 4% discrepancy between the drainage areas predicted by both the methods (**Figure 3.3**) amounting to 1.11×10^5 ft^3 of difference in drainage volumes. The difference between the predictions increases as the pressure front propagates farther in the reservoir, unlike the homogeneous case. Owing to the underestimation of drainage area by the SFM method, the pressure drops and Bourdet-type pressure derivative responses (**Figure 3.4**) are higher for the SFM method as compared to MFM method.

Table 3.4: Properties assumed for the case involving a vertical well in a heterogeneous reservoir with smoothly varying permeability distribution.

Reservoir property	
Dimension	*3,000 ft X 3,000 ft*
Grid size	*10 ft X 10 ft*
Permeability range	*0.005 - 0.075 md*
Porosity	*0.10*
Fluid property	
Viscosity	*1 cp*
Total compressibility	*1.0×10^{-6} psi^{-1}*
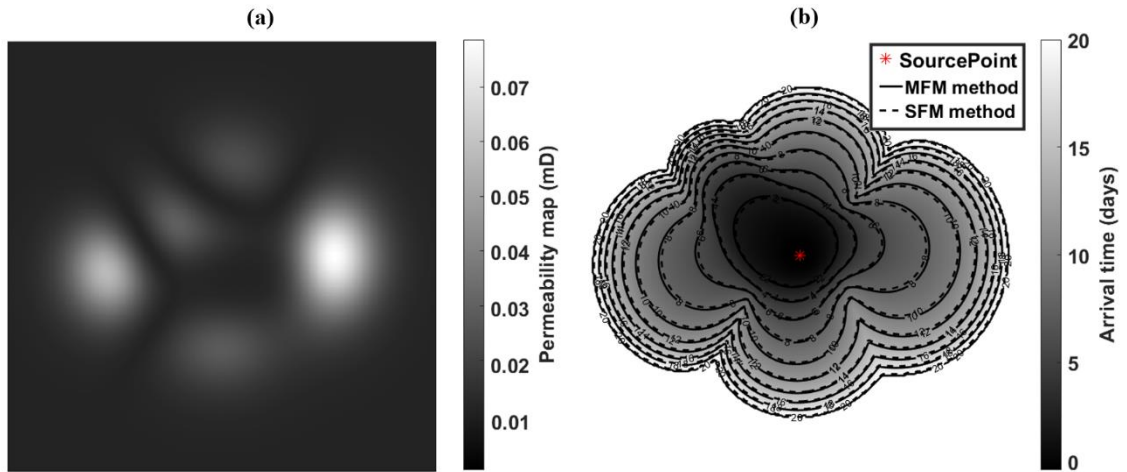
Figure 0.2: (a) Heterogeneous distribution of permeability and (b) ROI contour lines generated using SFM and MFM methods in a large reservoir spread across a 3,000-ft by 3,000-ft square-shaped area.
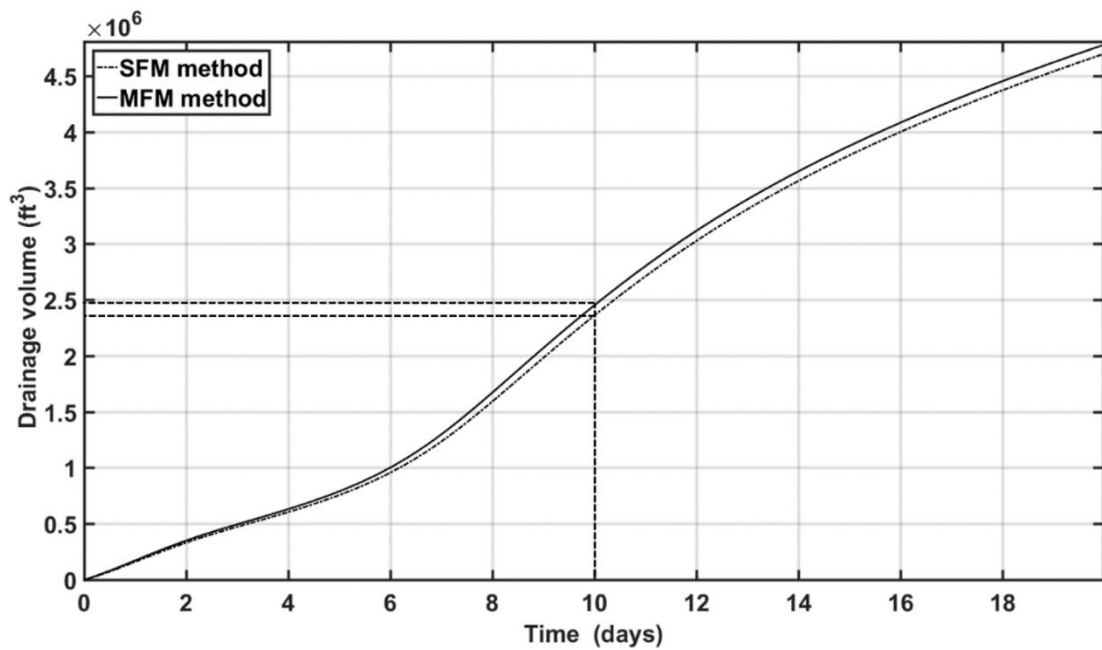
Figure 0.3: SFM and MFM predictions of time-varying drainage volumes in a large heterogeneous reservoir, as described in Figure 3.2, being produced using a vertical well.
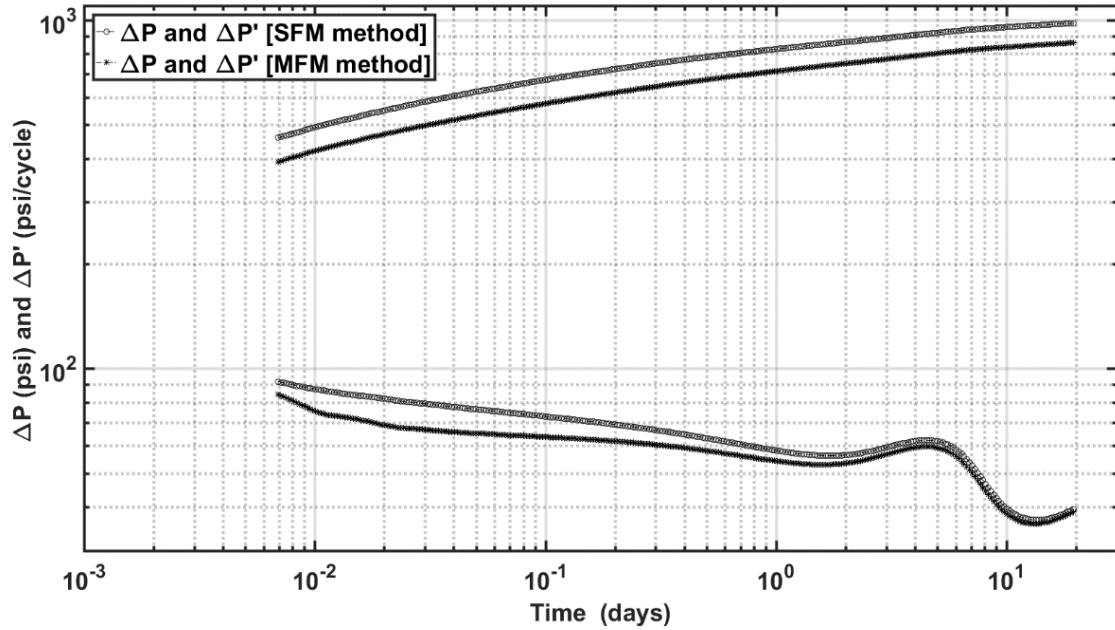
Figure 0.4: Diagnostic plot of pressure change and Bourdet-type pressure derivative responses of a vertical well in a large heterogeneous reservoir, as described in Figure 3.2, computed using SFM and MFM methods.

3.1.2 MFM method vs. Previously proposed method

In the cases of vertical well in a large reservoir (**Figure 3.5**) and fractured well in a bounded reservoir (**Figure 3.6**), our proposed second-order MFM predictions match well with those generated using the KAPPA analytical model. For the fractured well response, MFM accurately predicts the typical half-slope behavior in the pressure derivative response due to the presence of bi-wing planar fracture extending from the wellbore. Notably, when the reservoir is depleted because pressure front reaches the enclosing no-flow boundary, the pressure change and its derivative responses exhibit the unit slopes (**Figure 3.6**), which is a characteristic of a closed reservoir.

Neha et al. (2012) and Xie et al. (2012) implemented SFM method to estimate the pressure drop and its derivative responses observed in a centrally located vertical well in large homogeneous reservoir (**Figure 3.5**) and those in a centrally located vertical

fractured well in bounded reservoir (**Figure 3.6**). They demonstrated the efficacy of FM method as a pressure transient analysis tool using these cases. In order to validate and benchmark the MFM method that we developed and present in this thesis, we developed models similar to Neha et al. (2012) and Xie et al. (2012) and compared MFM predictions against their predictions. For the case of vertical well in large reservoir (**Figure 3.5**), **Table 3.5** lists the assumed reservoir, well and fluid properties. MFM method and SFM method (previously published model) generate similar pressure derivative responses. The pressure change response computed using the proposed MFM method agree very well with KAPPA analytical solutions, whereas a good agreement is not observed for the previously published SFM predictions. For the case of vertical fractured well in bounded reservoir (**Figure 3.6**), **Table 3.6** lists the assumed reservoir, well and fluid properties. In this case, the proposed second-order MFM method predicts pressure change and its derivative more accurately compared to the those predicted using the previously published models. Accuracy of MFM predictions is supported by their agreement with those generated using the KAPPA analytical solutions. Among the three methods, significant discrepancy in the pressure derivative response is exhibited by the previously published SFM method predictions especially beyond 10 days from the beginning of constant flow drawdown in the bounded reservoir (**Figure 3.6**). This figure also illustrates that the boundary effect on well response is observed at 10 days of production.

Table 3.5: Properties assumed for the case involving a vertical well in a large reservoir, described in Figure 3.5.

Reservoir property	
Dimension	*6,000 ft X 6,000 ft*
Grid size	*5 ft X 5 ft*
Initial pressure	*4500 psi*
Matrix permeability	*1 md*
Thickness	*10 ft*
Porosity	*0.25*
Well property	
Well radius	*0.25 ft*
Flowrate	*100 bbl/day*
Fluid property	
Viscosity	*0.4 cp*
Total compressibility	*6.0 X 10^{-6} psi^{-1}*
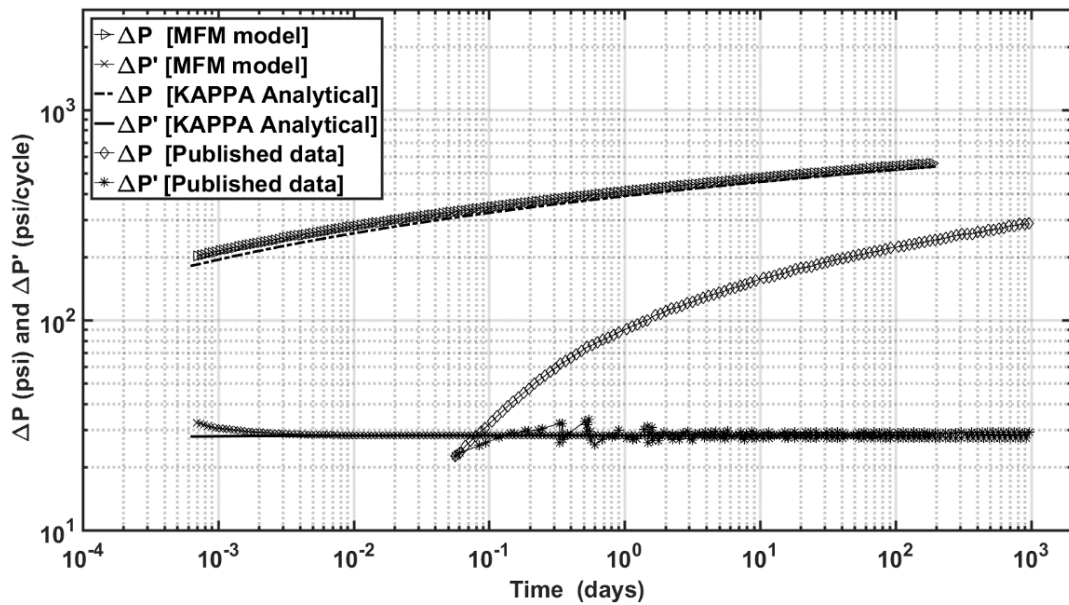
Figure 0.5: Diagnostic plot of pressure change and Bourdet-type derivative responses of a vertical well in a large homogeneous reservoir computed using MFM method, KAPPA Saphir analytical model, and previously published SFM model.

Table 3.6: Properties assumed for the case involving a vertical fractured well in a bounded reservoir, described in Figure 3.6.

Reservoir property	
Dimension	*2,000 ft X 2,000 ft*
Grid size	*1 ft X 1 ft*
Initial pressure	*4100 psi*
Matrix permeability	*1 md*
Thickness	*10 ft*
Porosity	*0.076*
Well/Fracture property	
Well radius	*0.25 ft*
Flowrate	*100 bbl/day*
Fracture half-length	*200 ft*
Fluid property	
Viscosity	*0.4 cp*
Total compressibility	*6.0 X 10^{-6} psi^{-1}*
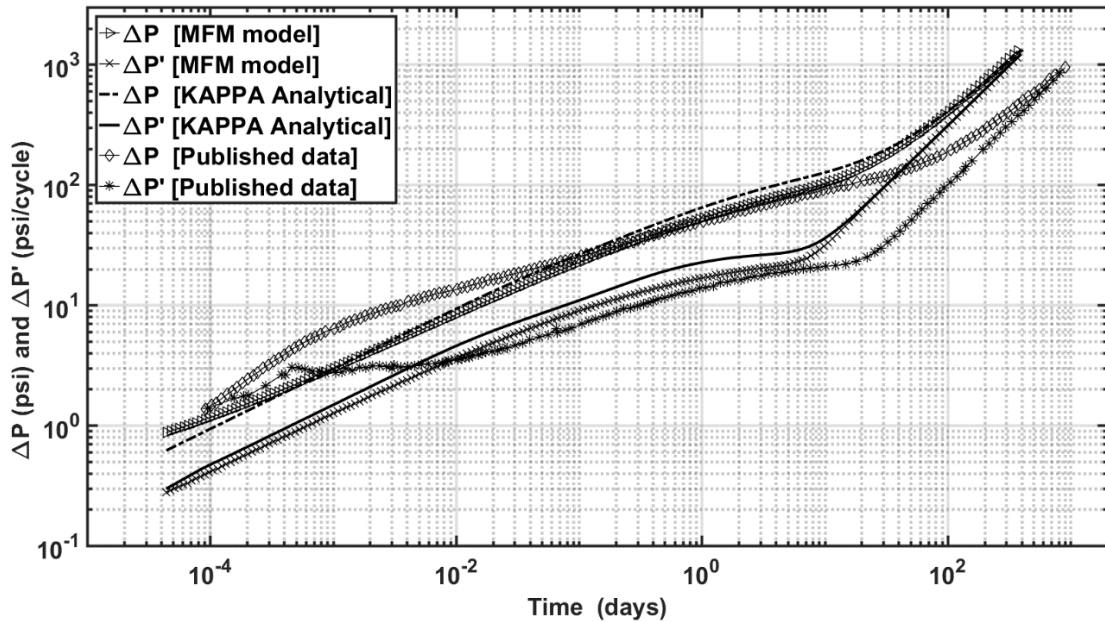
Figure 0.6: Diagnostic plot of pressure change and Bourdet-type derivative responses of a vertical well in a fractured reservoir computed using MFM method, KAPPA Saphir analytical model, and previously published SFM model.

3.1.3 MFM method vs. KAPPA analytical model vs. KAPPA numerical model

Computational complexity and accuracy of the proposed MFM method lies in between analytic methods and numerical models. Compared to numerical solutions, MFM method is faster and better accounts for heterogeneity in the reservoir diffusivity with a lower prediction accuracy. On the other hand, MFM method is more realistic with less simplifying assumptions compared to analytic solutions. Overall, MFM method can account for heterogeneity of reservoir properties and complexity of geometries and orientations without resorting to computationally intensive reservoir simulation or to simplifying assumptions of analytical models. To demonstrate the advantage of MFM method, we perform a numerical experiment using KAPPA software's numerical and analytic tools for pressure transient modeling. In this experiment, we attempt to predict another vertical fractured well response in a bounded reservoir using the properties listed in **Table 3.6**. **Figure 3.7** presents the results that allows a better comparison for the assessment of MFM accuracy compared to analytic and finite-difference numerical solutions. Noticeable discrepancies are observed in the pressure derivative responses among three methods during the radial flow regime lasting between 0.1 day to 10 days from the beginning of constant flow drawdown in the bounded reservoir. **Figure 3.7** illustrates that the boundary effect on well response is observed at 10 days of production. This example is too simple to discuss the computational efficiency. However, we can comment that three flow regimes, namely infinite conductivity fracture flow, infinitely acting radial flow, and closed reservoir flow, can be identified in all three methods. The effect of no-flow reservoir boundary in the MFM and KAPPA analytical methods tends to be well-identified compared to that in KAPPA numerical method. The number of grids

and nodes were equal in the MFM and KAPPA numerical models for this numerical experiment.
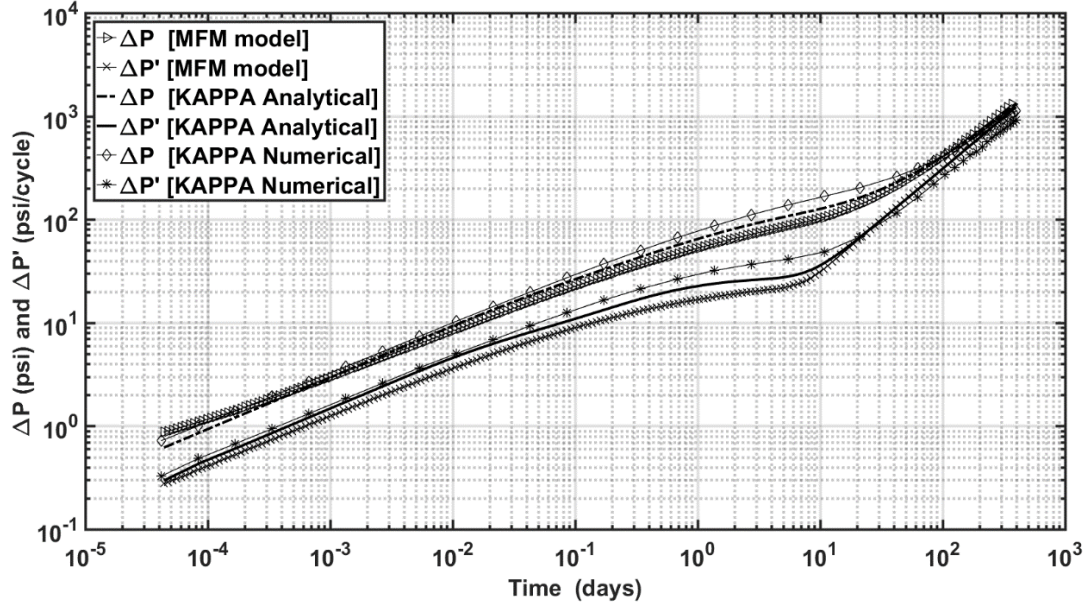
Figure 0.7: Diagnostic plot of pressure change and Bourdet-type derivative responses of a vertical fractured well in a bounded homogeneous reservoir, similar to that described in Figure 3.6, computed using MFM method, KAPPA Saphir numerical model, and KAPPA Saphir analytical model.

3.2 Validations of MFM method

3.2.1 Basic reservoir, Fluid, and Well Properties

In this section, validation of MFM method against KAPPA analytical model is performed for various reservoir scenarios, such as variation in matrix permeability, compressibility, flowrate, viscosity, wellbore radius, porosity, reservoir size, and fracture half length (**Figures 9 and 10**). We undertake this extensive validation work because there is no literature on the efficacy of MFM method for a wide range of reservoir scenarios. Overall, the proposed MFM method generates accurate results. Prediction accuracy for well with finitely conductive bi-wing fractures is poor compared to those

for other properties presented in **Figures 9 and 10**. Implementation of fracture width in

corner-point grid scheme, as adapted in MFM method, needs to be improved with grid

refinement to improve the accuracy for finite fracture conductivity.
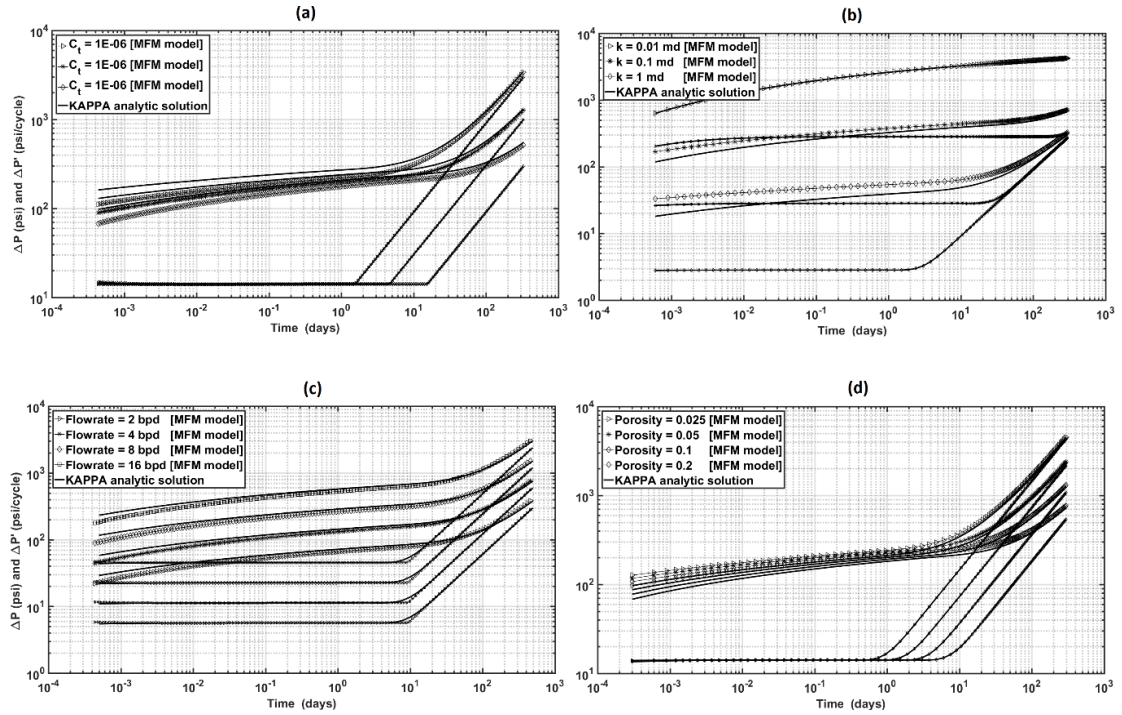
Figure 0.8: Diagnostic plot of pressure change and its derivative responses of a vertical well in a bounded homogeneous reservoir for various (a) compressibility, (b) permeability, (c) flowrate, and (d) porosity computed using MFM method.
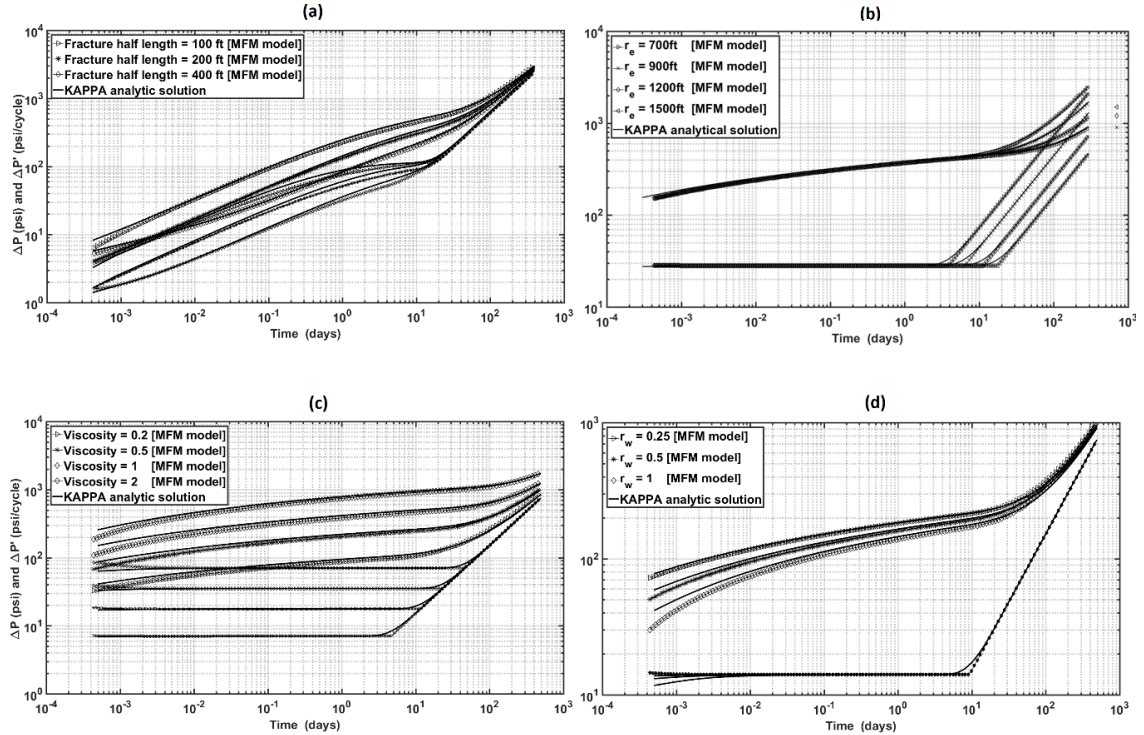
Figure 0.9: Diagnostic plot of pressure change and its derivative responses of a vertical well in a bounded homogeneous reservoir for various (a) fracture half length, (b) reservoir size, (c) viscosity, and (d) well radius computed using MFM method.

3.2.2 Geometry of Reservoir Boundary

For purposes of validation, we consider four geometries of no-flow reservoir boundary, namely (a) partially circular no-flow reservoir boundary with single sealing linear fault, (b) partially circular no-flow reservoir boundary with two parallel sealing linear faults, (c) partially circular no-flow reservoir boundary with two perpendicular intersecting sealing linear faults, and (d) square-shaped no-flow reservoir boundary (**Figure 3.10**).

27
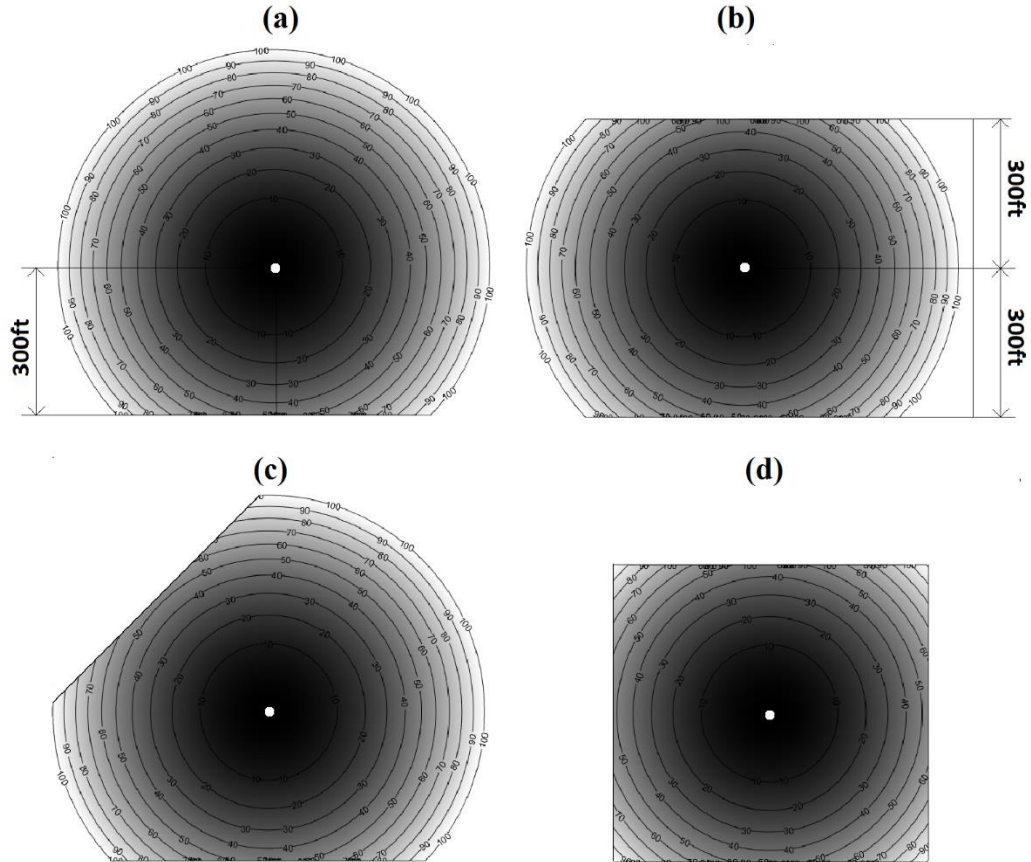
Figure 0.10: Travel-time computed using MFM method at $t = 100$ **days for four distinct reservoir boundary shapes, namely (a) partially circular no-flow reservoir boundary with single sealing linear fault, (b) partially circular no-flow boundary with two parallel sealing linear faults, (c) partially circular no-flow reservoir boundary with two perpendicular intersecting sealing linear faults, and (d) square-shaped no-flow reservoir boundary.**

We present the validation of MFM predictions against KAPPA Rubis numerical simulation for each case with different boundary shapes in **Figure 3.11**. The duration of radial flow regime depends on the distance of no-flow boundaries from wells. After the end of radial flow regime, characteristic signatures of the reservoir boundary shapes are observed in both MFM and KAPPA predictions. In the presence of rectangular no-flow boundary (Case d) and channel-type two parallel no-flow boundaries (Case b), the derivative response shows the characteristic unit slope and half slope, respectively, as shown in **Figure 3.11**. Furthermore, in the presence of single sealing fault (Case a) and

28

two intersecting sealing faults (Case c), the derivative response stabilizes at twice and four-times, respectively, of its value attained during the radial flow regime, as shown in **Figure 3.11**, which is characteristic of two sealing faults at various orientations
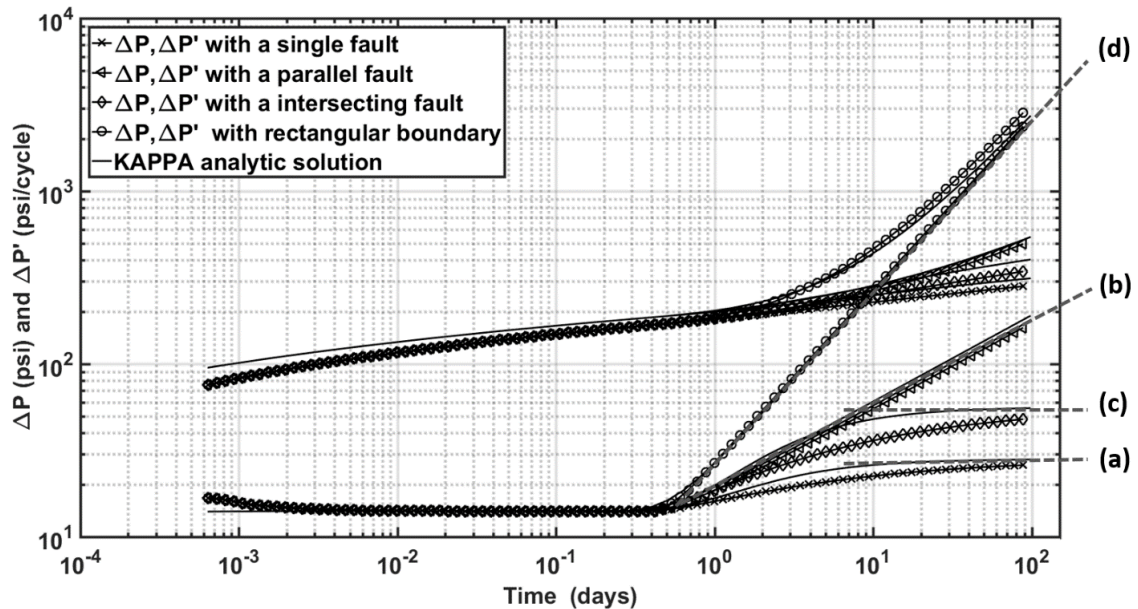
Figure 0.11: Travel Diagnostic plot of pressure change and its derivative responses of vertical wells in reservoirs having various boundary shapes, as described in Figure 3.10, computed using MFM method.

3.2.3 Effect of Fractures

MFM method can be effectively used to estimate pressure response not only in homogeneous reservoir with heteromorphous geometry of no-flow boundary but also in heterogeneous reservoir affected by permeability/porosity distribution and in the presence of induced/natural fractures. In unconventional reservoirs, it is crucial that reservoir simulation and pressure front tracking account for the effect of induced fracture and complex natural fracture network in the reservoir to quantify the interactions of hydraulic fractures and natural fractures with pressure front. These interactions govern the drainage volume. We test the accuracy of MFM method for reservoirs with complex fracture geometries and conductivity distribution being produced from a vertical

fractured well. Temporal variations of drainage volume in such reservoirs are studied using following three scenarios:
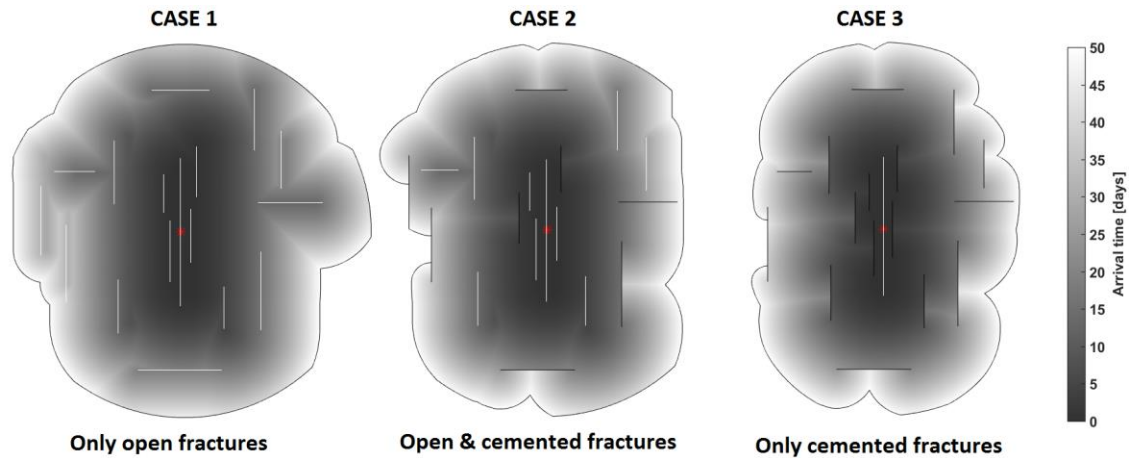
Figure 0.12: Travel Diagnostic MFM predictions of travel-time contour lines till t **= 50 days for three naturally fractured reservoirs of varying conductivity being produced from a vertical fractured well.**

- Case 1: A reservoir with only infinite conductivity fractures (**Figure 3.12a**)

- Case 2: A reservoir with both cemented natural fractures and infinite

  conductivity fractures (**Figure 3.12b**)

- Case 3: A reservoir with only cemented fractures. (**Figure 3.12c**)

As can be seen in **Figure 3.13**, Case 3 has smallest drainage area and highest-pressure depletion. Time-varying drainage area stabilizes for Case 1 around 60 days and it takes 120 days for Case 3. Differences in the pressure propagation and travel time due to the difference in cemented- and open-fracture distributions are visible in **Figure 3.12**. The presence of open fractures permits a fast propagation of pressure, which is not possible in the presence of closed fractures. Pressure propagation in Case 3 was also simulated using KAPPA Rubis numerical simulator (**Figure 3.14**). Overall, there is a qualitative agreement between MFM and KAPPA Rubis predictions. However, the effect of reservoir boundary is not evident in KAPPA Rubis results, which is adequately

captured as the unit slope signature of the pressure derivative response in MFM predictions
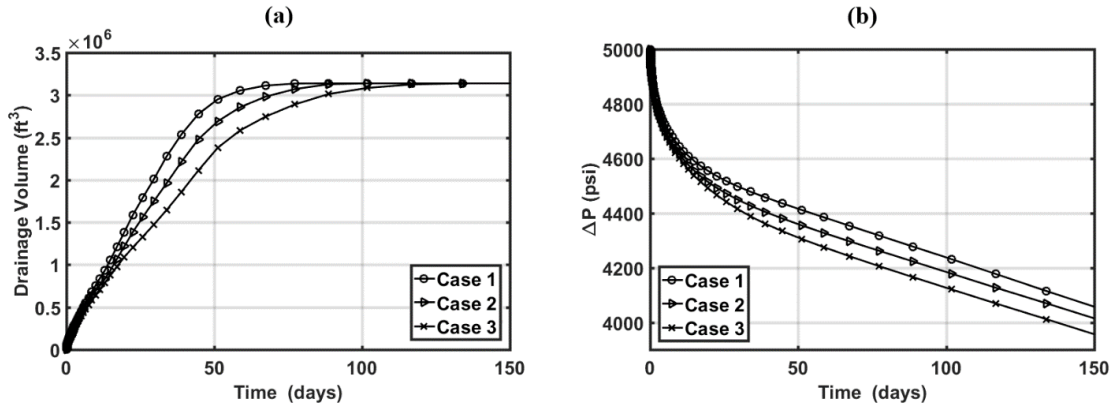
Figure 0.13: MFM predictions of (a) time-varying drainage volumes and (b) pressure change responses of vertical fractured wells in three naturally fractured reservoirs, as described in Figure 3.12.
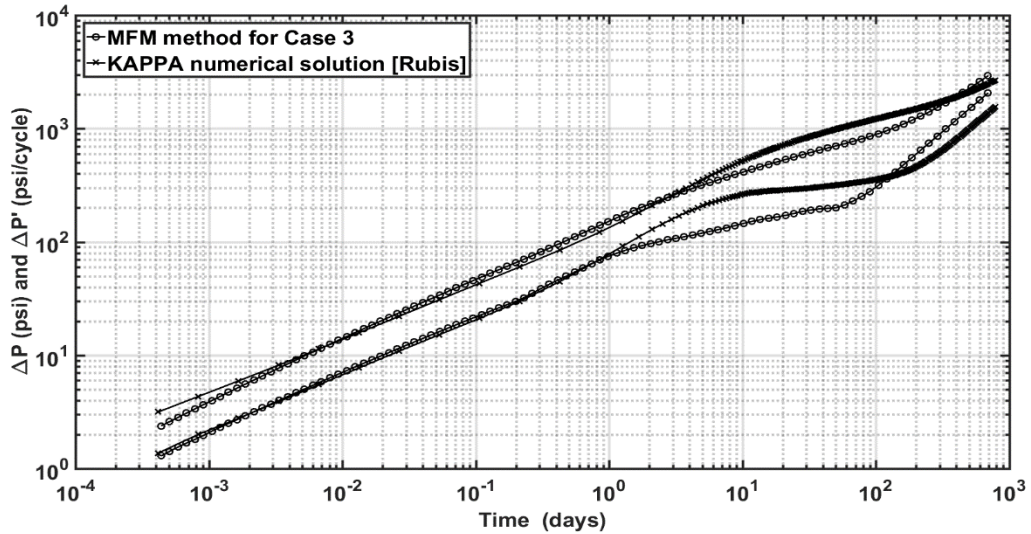
Figure 0.14: Diagnostic plot of pressure change and its derivative responses of a vertical fractured well in a naturally fractured reservoir, as shown in Case 3 of Figure 3.12, computed using MFM method and KAPPA Saphir numerical model.

3.2.4 Well Interference Effects

MFM method can be used to model superposition in space and in time provided the system exhibits linear behavior. Algorithm used in previous sections needs to be

modified to consider superposition principle. Using the new algorithm, the estimated

drainage volume attributes the pressure drop and its derivative for multi-well scenario.

Superposition in space requires that the propagation of pressure front for each well is

modeled using MFM method separately in the absence of other wells, with an assumption

that there is no effect from adjacent wells. The drainage volume calculated using the

MFM method is used to compute the pressure changes at any point in the reservoir due

to each well, which is then added to obtain the total pressure change in the multi-well

scenario. Superposition in space is valid when the entire system exhibits negligible non-

linear flow behavior, for example, absence of turbulence and non-linear pressure

dependence of reservoir and fluid properties. MFM method was tested for a case with

producing well located 50-ft away from the observation well (**Figure 3.15**). MFM

predictions of pressure and its derivative responses match well with KAPPA analytical

and numerical predictions (**Figure 3.16**).
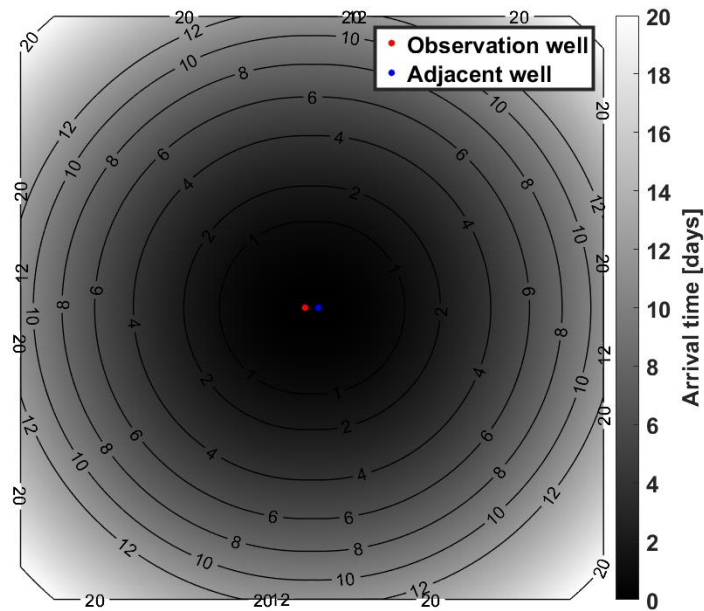
Figure 0.15: MFM travel-time predictions of two producing vertical wells 50-ft away from each other in a square-shaped bounded homogeneous reservoir.

32
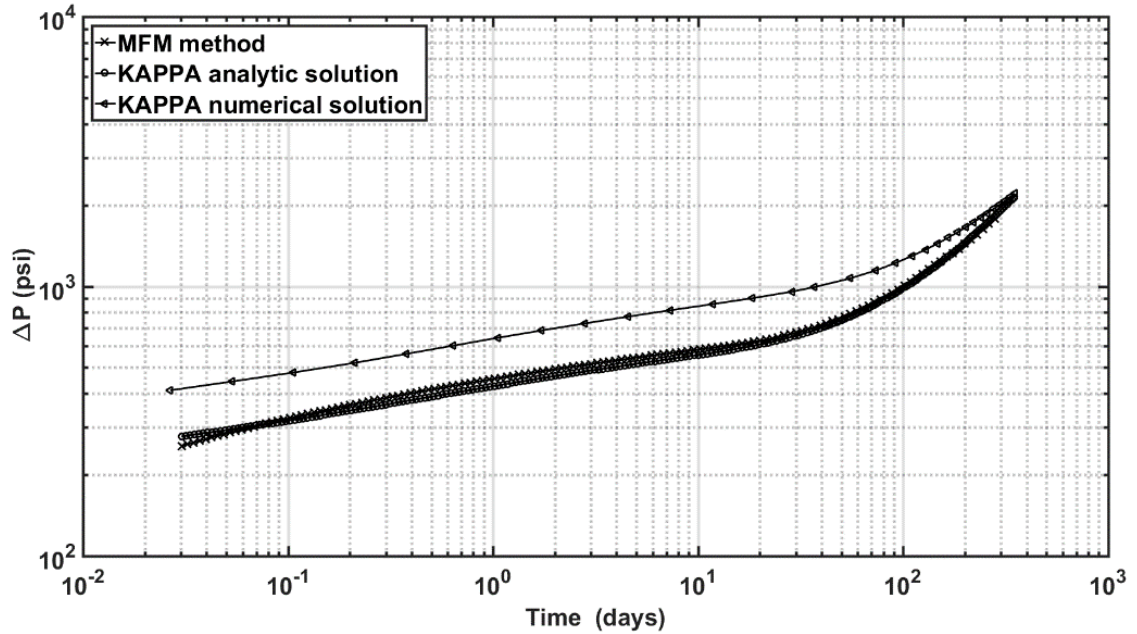
Figure 0.16: Diagnostic plot of pressure change and its derivative responses of a vertical well 50-ft away from another vertical well in a square-shaped bounded homogeneous reservoir, as described in Figure 3.15, computed using MFM method, KAPPA Saphir analytical model, and KAPPA Rubis numerical model.

3.3 Conclusions

In this chapter, we tested an accurate and efficient method for pressure responses and validated intensively in KAPPA numerical solutions for various fractured heterogeneous reservoir scenarios. The reservoir drainage volume can be estimated from the pressure 'front' propagation using multistencils fast marching (MFM) method. A geometric approximation of the drainage volume is then used to compute the well rates and the reservoir pressure. MFM Method proves to be computationally efficient in characterizing the effects of reservoir and fracture properties on pressure transient response in complex reservoirs. This method can effectively give an intuitive clue for not only reservoir behavior but design process of hydraulic fracture or well spacing.

33

CHAPTER 4: MULTISTENCILS FAST MARCHING IN THE PRESENCE OF ZONES OF HIGH-CONTRAST DIFFUSIVITIES

In previous chapters, multistencils fast marching method is implemented in heterogeneous reservoirs with smoothly varying permeability distribution and containing thin infinite- and zero-conductivity fractures. The proposed modeling method was validated against analytic and numerical results. In this chapter, the MFM method is improved further to model reservoirs with high-contrast permeability distribution and large-sized low-permeability zones, which were erroneously modeled using the MFM method as proposed in the previous chapter.

4.1 Literature Review

Extensive studies have been conducted on tracking wave propagation front, propagation path and its speed in highly heterogeneous medium (Dey et al., 2009; Capozzoli et al., 2014). These studies include the conventional fast marching (FM) techniques to find the first-arriving phase as well as the recent developments to employ the reflection of wave propagation in the FM method (Rawlinson and Sambridge, 2004). FM method is a popular numerical tool in petroleum engineering to determine the drainage volume in highly heterogeneous reservoirs, such as shale formation with discrete fracture network (Kim et al., 2009; Kang et al., 2013; Yang et al., 2017) Current analysis on the reservoir drainage volume using FM method involves relatively low-contrast or smoothly varying permeability distribution in the reservoir. Presence of high-contrast permeability heterogeneity in the medium challenges the computation of drainage volume. In this chapter, MFM method is improved to estimate realistic drainage volume in reservoirs with spatially distributed zones of high-contrast diffusivities. The

accuracy of the proposed method is evaluated by comparing the MFM predictions against those of KAPPA Rubis numerical simulator.

4.2 Problem Statement

There are numerous publications on fracture analysis and reservoir performance characterization in spatially heterogeneous hydrocarbon reservoirs. FM-based methods facilitate interpretation of pressure transient responses to estimate reservoir volume and flow parameters. FM method predictions have been validated for reservoirs with high-conductivity induced fractures and sealed natural fracture. The MFM method that we developed and described in Chapter 3 tracks down the propagation of outermost pressure front and subsequently enables computation of the drainage volume in ideal reservoirs without large-sized areas of high permeability contrasts. MFM simulations for reservoirs containing cemented/conductive fractures accurately predict the propagation of pressure response because the volume of fractures compared to the reservoir volume is negligible. However, MFM method developed so far is prone to numerical dispersion and errors with an increase in the number of the fractures and the volume occupied by zones of high contrast.

We improve the MFM method and describe the improvements and algorithmic changes in this chapter. For example, **Figure 4.1b** shows the pressure front propagation at 5 days in the square-shaped bounded reservoir with an impermeable patch (**Figure 4.1a**) being produced from a centrally located vertical well. The two solid lines in **Figure 4.1b** represent the pressure fronts, wherein the outer front describes the extent of pressure propagation in the bounded reservoir and the inner front indicates that pressure and flow is not able to penetrate the impermeable patch in the reservoir at the 5th day of production.

The improved MFM algorithm captures the effect of impermeable patch on the drainage volume.

(a)   **(b)**
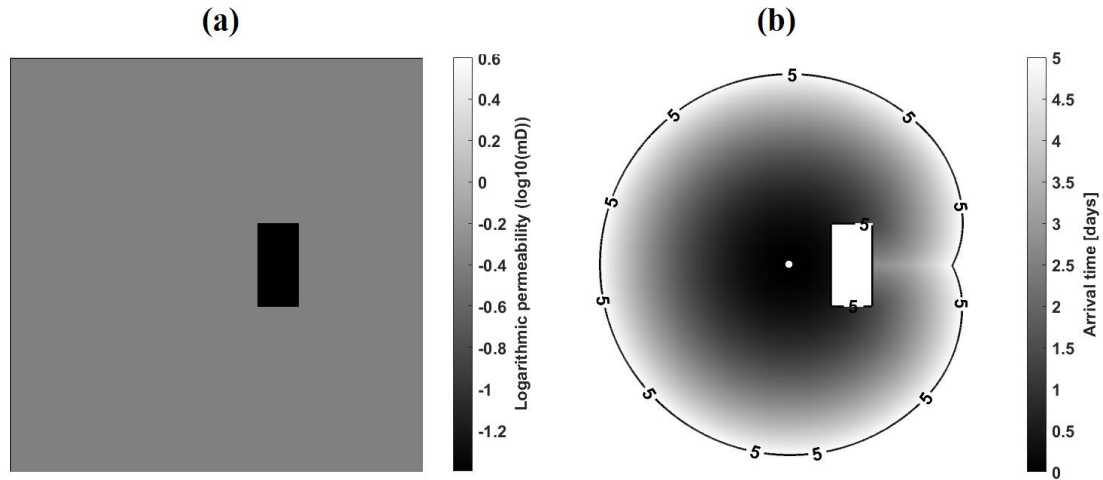
Figure 0.1: (a) distribution of permeability in logarithmic scale with a 100-ft by 200-ft size impermeable zone and (b) depth of investigation (DOI) contour line at $t = 5$ days in a large reservoir spread across a 1000-ft by 1000-ft square-shape area.

Similar challenges are encountered in a low-permeability reservoir containing several highly conductive (or resistive) pathways, as shown in **Figure 4.2a**. Application of the MFM method described in Chapter 3 generates numerical noise in the calculation of pressure derivative response, as shown in **Figure 4.3a**. These noisy computations are primarily due to the erroneous calculations of drainage area due to the large number of fractures with large permeability contrast with respect to the reservoir. The usefulness of the improved MFM method is presented in **Figure 4.3b**, in which the pressure derivative response is free from fluctuations that indicate accurate accounting of the presence of high-contrast fractures in the reservoir (**Figure 4.2a**).
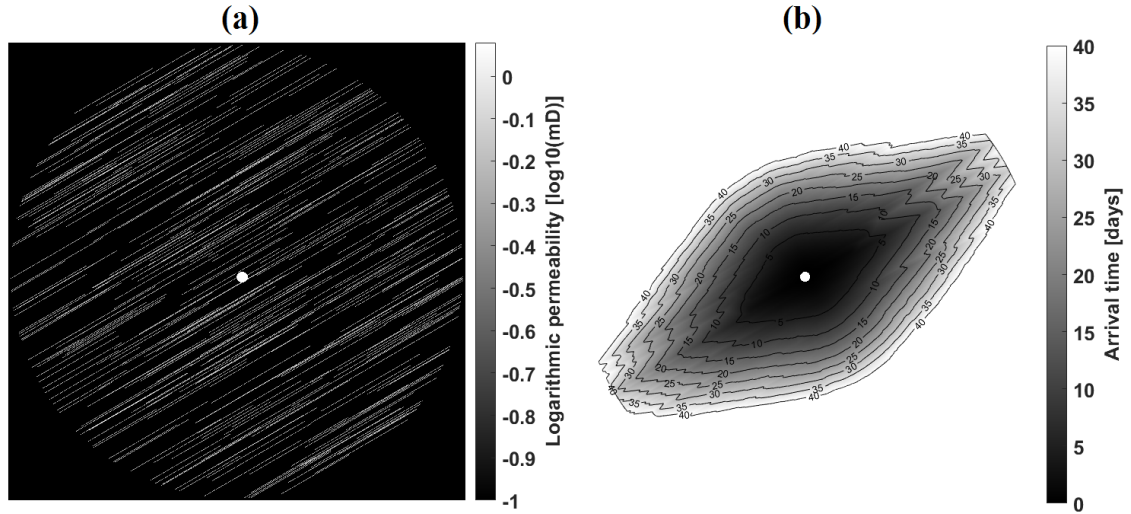
Figure 0.2: (a) High permeability contrast map of a vertical well in a circular-shaped bounded heterogenous reservoir and (b) travel-time computed using MFM method at $t = 40$ days.
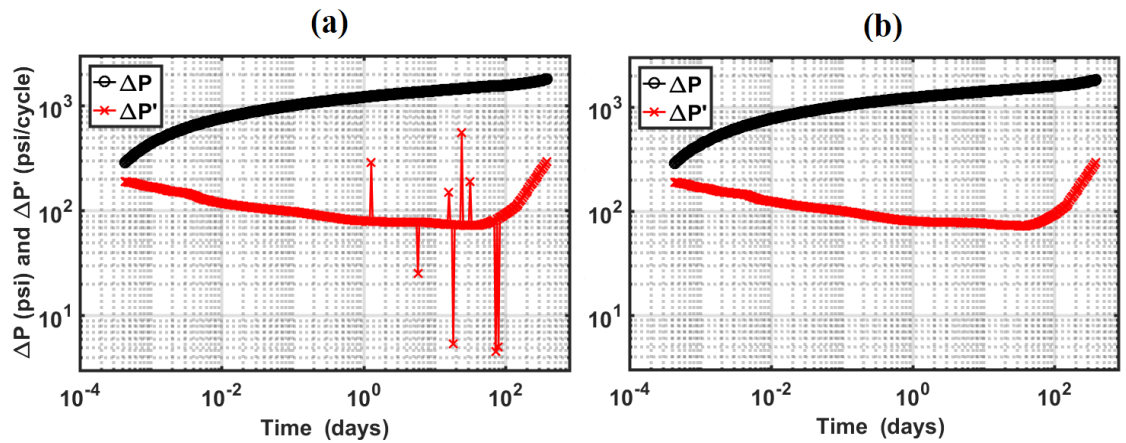
Figure 0.3: Diagnostic plot of pressure changes and Bourdet-type derivative responses of a vertical well in the bounded heterogeneous reservoir, as described in Figure 4.2a, computed using (a) the previous MFM algorithm and (b) improved MFM algorithm.

4.3 Improved MFM Method

The new MFM algorithm to generate the drainage volume and pressure diagnostic plots is descried in **Figure 4.4**. First, reservoir and fluid properties, such as porosity, permeability, total compressibility, and viscosity, and numerical discretization parameters are defined by the user. Following that, diffusivity speeds are calculated for

all the grids representing the reservoir. Based on the diffusivity speed map, MFM method is invoked to compute the Diffusivity Time of Flight (DTF), as described in Chapter 3. Once the DTF is determined for all the grids, the simulator creates the contour lines for each time step by connecting nodes of equal DTF. Drainage volume is then calculated using the inner area of each contour line. Pressure diagnostic plot can be generated by integrating the drainage volume as a function of time using Equation 2.35 with the assumption of a constant rate drawdown in a vertical well. When the boundaries of large-sized zones of high permeability-contrast are encountered, the pressure front makes a detour around low permeability zone. Once the pressure front finishes a detour, the pressure front creates two enclosed pressure fronts, one expanding outwards and the other surrounding low permeability zone. The improved front tracking algorithm can distinguish those multiple enclosed pressure fronts one by one. The areas of identified high-contrast zones are subtracted from the total inner area of the outermost pressure front for a specific time to obtain an accurate drainage area.
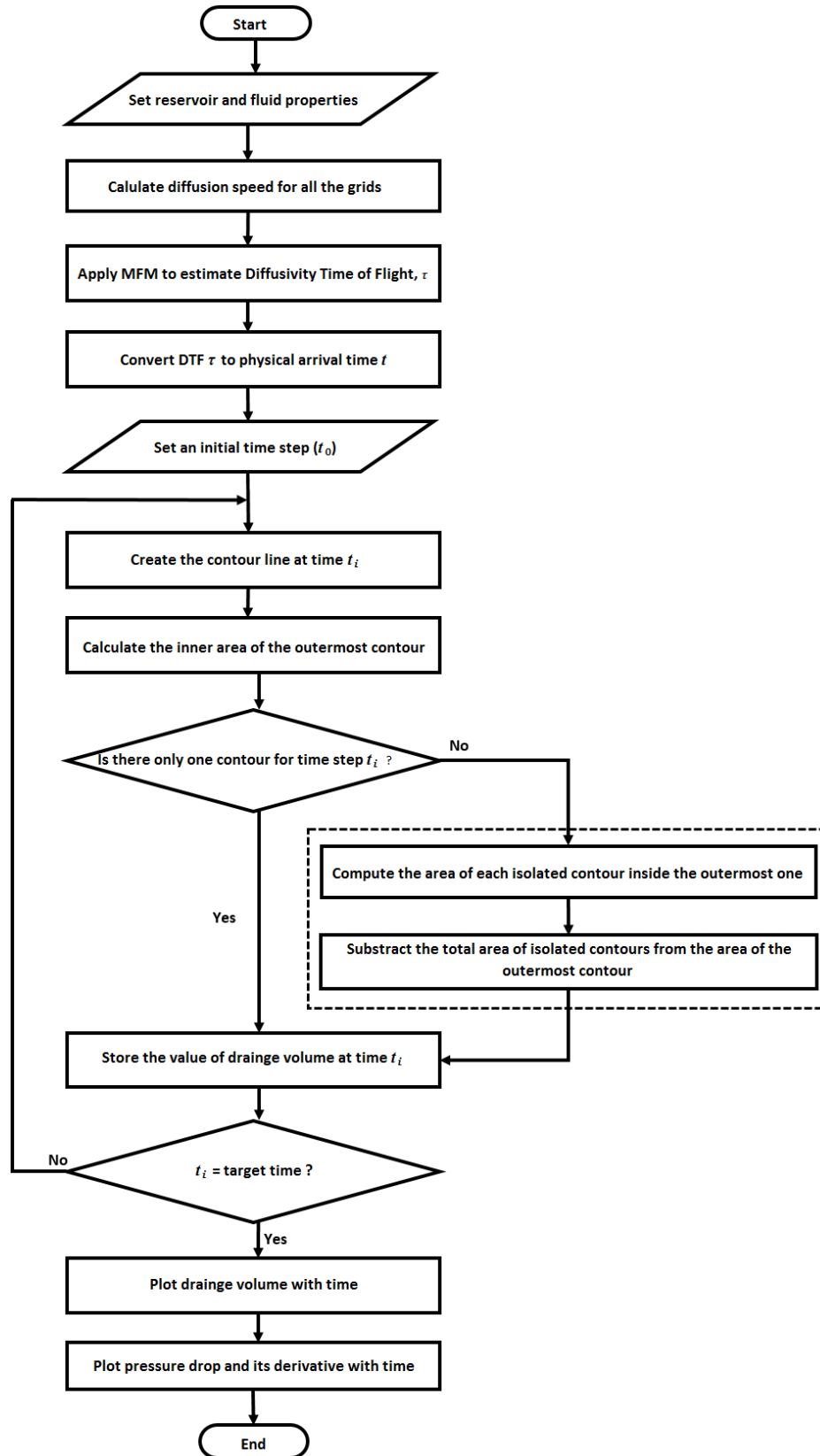
Figure 0.4: Flow chart of the improved multistencils fast marching method.

4.4 Improved MFM Predictions

Efficacy of the improved MFM method in comparison to the earlier one is demonstrated on the reservoir model shown in **Figure 4.5a**. The propagation of front is modeled in **Figure 4.5b**, in which the front starts enveloping the high-contrast patch on the fifth day of production and completely envelopes the patch close to 35th day of production. The new algorithm generates smoothly varying drainage volume, unlike the abrupt change observed around 38th day of production when using the previous code (**Figure 4.6**).
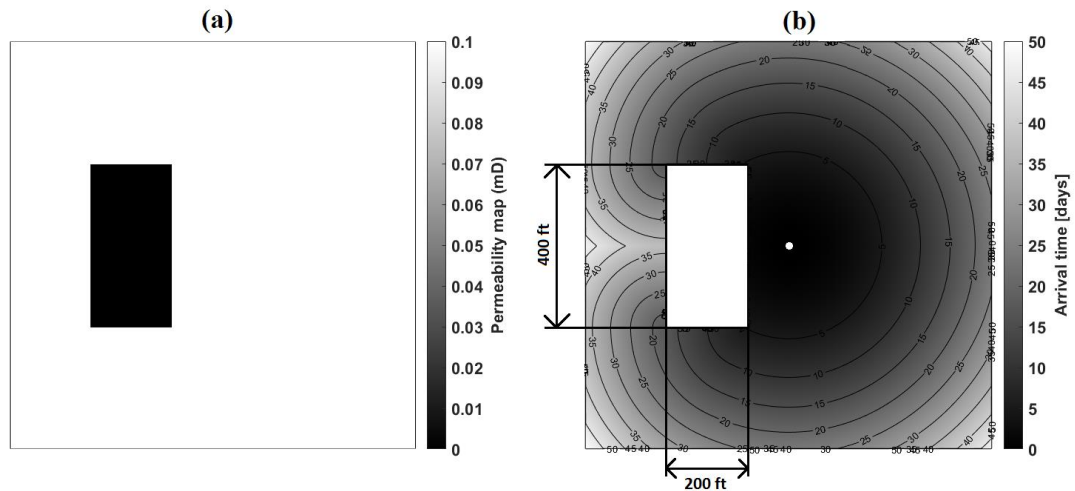
Figure 0.5: (a) Distribution of permeability in logarithmic scale and (b) diffusive time of flight contour lines at various times for a bounded reservoir spread across a 1000-ft by 1000-ft square-shaped area with a low-permeability 400-ft by 200-ft rectangular zone being produced from a centrally located vertical well.
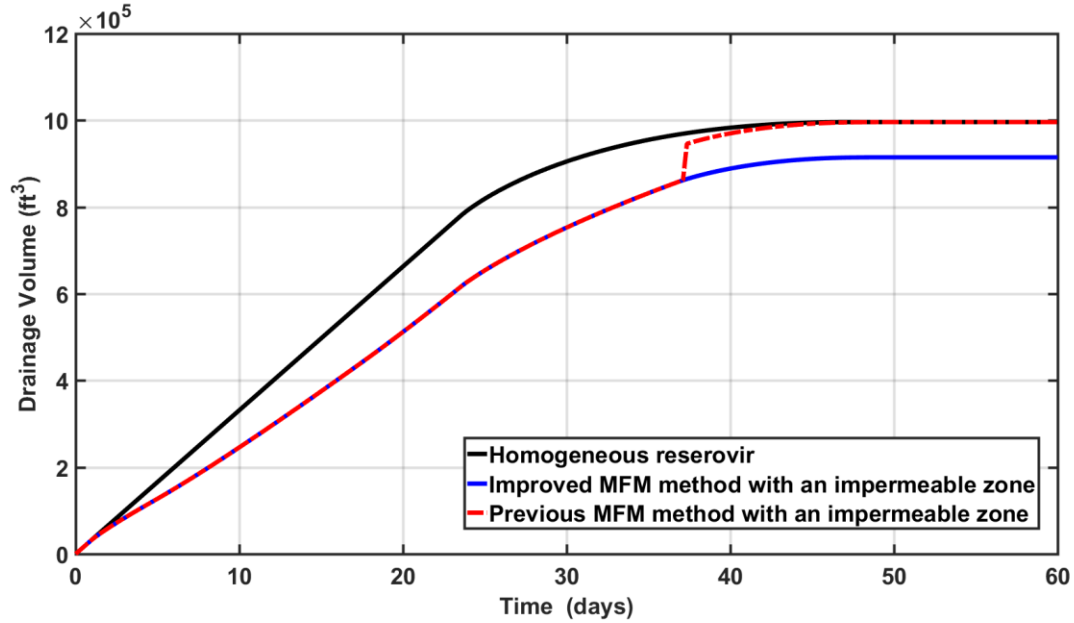
Figure 0.6: Time-varying drainage volume computed using previous and improved MFM methods for the bounded reservoir shown in Figure 4.5a.

Next, the improved MFM algorithm is evaluated on reservoirs containing various shapes of isolated high-contrast zones. Various cases include square, circle, triangle, and L-shaped regions (**Figure 4.7**) of low permeability that exhibits high contrast with respect to reservoir permeability. The computed drainage volumes for the four cases are plotted simultaneously as a function of time till the pressure front reaches the no-flow rectangular boundaries (**Figure 4.7**). In **Figure 4.8**, all the time-varying drainage volumes are plotted including one for the homogeneous reservoir without any high-contrast zone, identified using black curve. All computed curves are smooth, and the late-time stable drainage area decreases with the increase in isolated high-contrast shapes having extremely low permeability. In **Table 4.1**, The late-time stable drainage volumes calculated using the improved MFM method are compared against the expect values based on model geometry. The table indicates greater than 99.5% accuracy in the new MFM predictions of late-time drainage volumes for various reservoir models. Presence

of these zones result in a significant alteration in the pressure front propagation beyond their locations. In **Figure 4.8**, the time for stabilization of the time-varying drainage volumes increases with increase in number of isolated high-contrast zones of low permeability, which indicates that these zones impede the overall front propagation. Case 3 stabilizes 10 days after the stabilization of the homogeneous case without any isolated high-contrast zones.
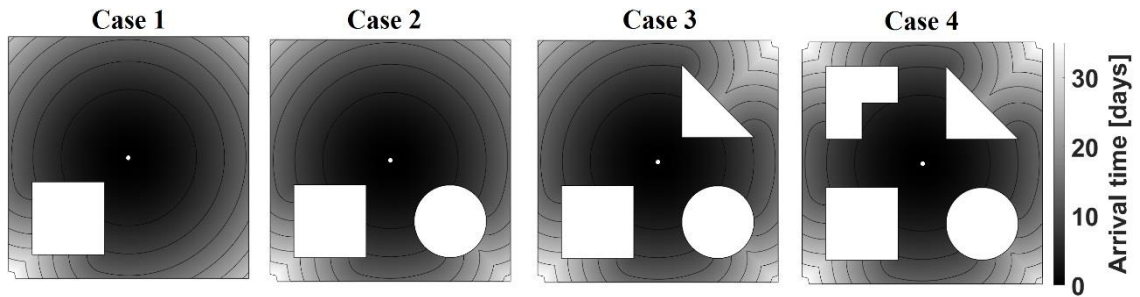
Figure 0.7: Diffusive time of flight contours computed using the improved MFM method in bounded rectangular reservoirs with distinct high-contrast zones of low permeability.
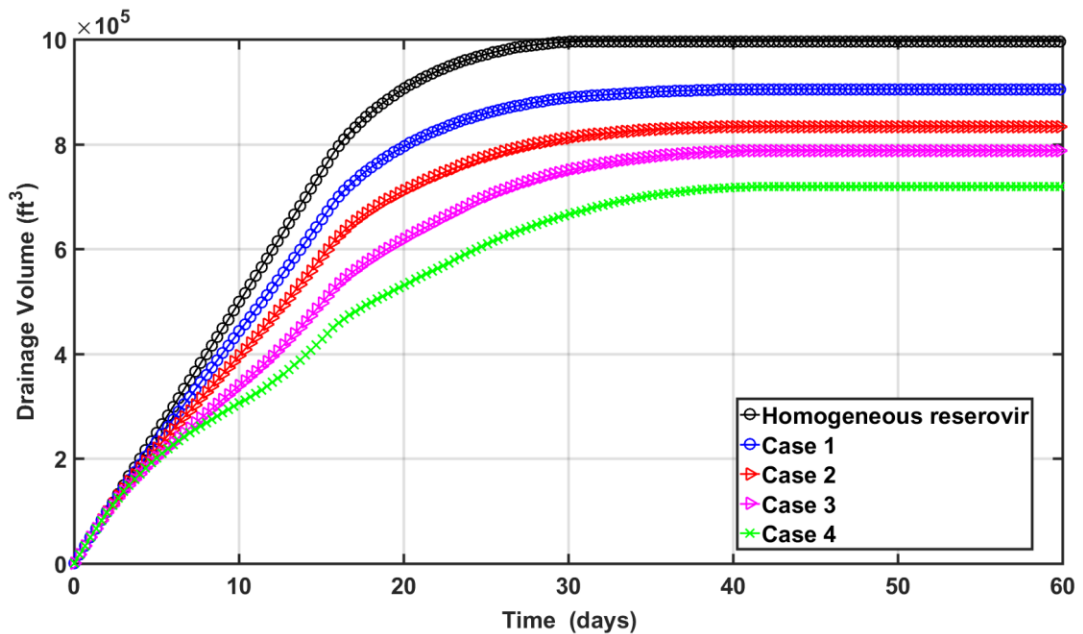
Figure 0.8: Time-varying drainage volumes calculated using MFM method in bounded rectangular reservoirs with distinct high-contrast zones of low permeability.

Table 4.1: Late-time drainage areas predicted using MFM method against the total reservoir area based on the model geometry as shown in Figure 4.7.

	Homogeneous	Case 1	Case 2	Case 3	Case 4
Expected value	*1,000,000 ft²*	*910,000 ft²*	*839,314ft²*	*794,314 ft²*	*726,814 ft²*
Estimated value	*1,000,000 ft²*	*908,798 ft²*	*837,692 ft²*	*791,790 ft²*	*723,089 ft²*

4.5 Validation of the Improved MFM Method

For purposes of validation, MFM predictions are compared against KAPPA Rubis numerical simulation, KAPPA Saphir analytical, and CMG numerical simulation results. The pressure change and pressure derivative responses obtained using MFM method are compared against those obtained using KAPPA numerical simulator, KAPPA analytical model, and CMG simulator for bounded reservoirs with isolated high-contrast zones. Notably, the KAPPA and MFM predictions have agreeable responses, whereas CMG and MFM predictions exhibit discrepancies.

4.5.1 MFM method vs. KAPPA Rubis simulator vs. KAPPA Saphir simulator

This comparison was done for bounded reservoir spread across 1000-ft by 1000-ft square-shaped area with two 100-ft by 200-ft rectangular-shaped high-contrast zones of low permeability being produced using a centrally located vertical well (**Figure 4.9**). Other input properties used are listed in **Table 4.2**. The pressure and its derivative responses computed using KAPPA numerical simulator closely match those obtained with MFM method (**Figure 4.10**). Bourdet-type pressure derivative responses obtained using the two simulators diverge from 2 days to 50 days of production until the start of closed boundary flow exhibited by a unit slope. We claim that the drop in the pressure derivative as predicted by MFM method is more realistic than KAPPA numerical result

because the MFM predicted drop in the derivative indicates absence of an infinite no-flow boundary and it happens primarily because of pressure front takes a certain time to engulf the high-contrast low-permeability zone. Once that zone is engulfed the pressure derivative drops down from the sealing-fault-like response.

Table 4.2: Properties assumed for the case involving a vertical well in the bounded reservoir described in Figure 4.9.

Reservoir properties	
Dimension	*1,000 ft X 1,000 ft*
Grid size	*1 ft X 1 ft*
Initial pressure	*5000 psi*
Matrix permeability	*0.15 md*
Thickness	*10 ft*
Porosity	*0.1*
Well property	
Well radius	*0.25 ft*
Flowrate	*5 bbl/day*
Fluid property	
Viscosity	*0.4 cp*
Total compressibility	*6.0 X 10^{-6} psi^{-1}*
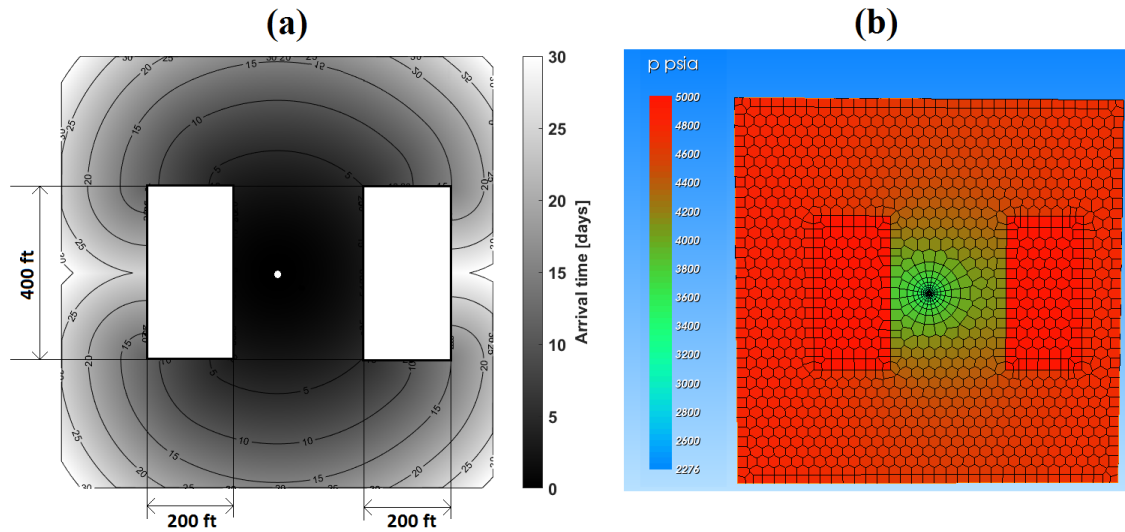
Figure 0.9: (a) Diffusive time of flight contours and (b) KAPPA Rubis simulation of reservoir pressure at t = 100 days in across 1000-ft by 1000-ft square-shaped bounded reservoir with two 100-ft by 200-ft rectangular-shaped high-contrast zones of low permeability.
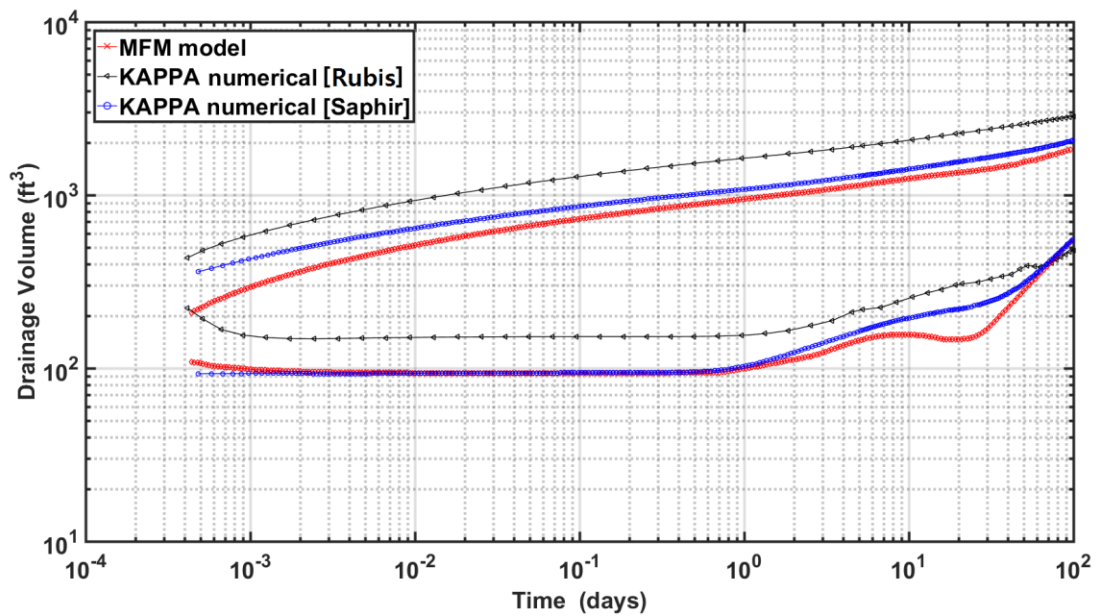
Figure 0.10: Diagnostic plot of pressure change and Bourdet-type pressure derivative responses of a vertical well in a bounded rectangular reservoir, shown in Figure 4.9, computed using MFM method, KAPPA Saphir, and KAPPA Rubis numerical simulation.

4.5.2 MFM method vs. CMG vs. KAPPA Saphir numerical model

This comparison was done for bounded reservoir of 0.5 mD permeability spread across 1000-ft by 1000-ft square-shaped area with four 100-ft by 400-ft rectangular-shaped zones of permeability 0.05 mD, 0.005 mD, 0.0005 mD, and 0.00005 mD, respectively, being produced using a centrally located vertical well (**Figure 4.11**). Other reservoir and fluid properties are listed in **Table 4.3.** In **Figure 4.11b**, the propagation front is able to completely move through the 0.05 mD zone on the 8th day, whereas for the 0.005 mD zone the front is able to propagate only one-fourth of the width into that zone. Zones with 3-order of permeability contrast with respect to the host medium behave as impermeable zones in this scenario. Pressure and derivative responses computed using MFM method and KAPPA numerical simulator are in good agreement (**Figure 4.12**). For CMG simulations, single phase production and constant fluid properties were set to consistently compare the CMG results with MFM predictions. The computed pressure drops and it derivative responses obtained using CMG significantly deviates from those computed using MFM method and KAPPA simulator after 1 day of production, when the pressure front reaches the surrounding low-permeability zones (**Figure 4.12**).

Table 4.3: Properties assumed for the case involving a vertical well in a bounded reservoir, described in Figure 4.11.

Reservoir properties	
Dimension	*1,000 ft X 1,000 ft*
Grid size	*1 ft X 1 ft*
Initial pressure	*5000 psi*
Matrix permeability	*0.5 md*
Thickness	*10 ft*
Porosity	*0.1*
Well property	
Well radius	*0.25 ft*
Flowrate	*1 bbl/day*
Fluid property	
Viscosity	*0.4 cp*
Total compressibility	*$6.0 \times 10^{-6} psi^{-1}$*
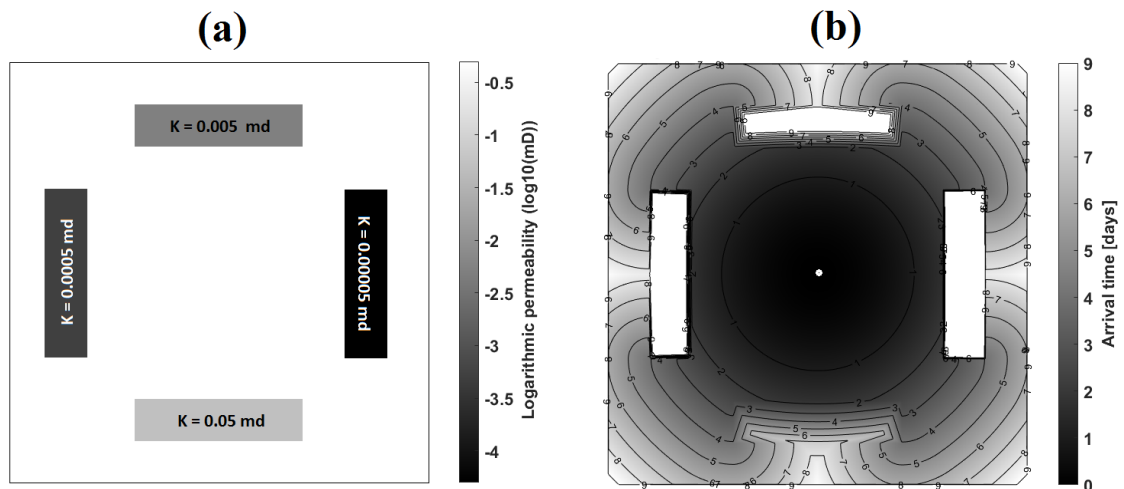
Figure 0.11: (a) Distribution of permeability in logarithmic scale and (b) diffusive time of flight contours in a bounded reservoir spread across a 1000-ft by 1000-ft square-shaped area with four low-permeability 100-ft by 400-ft rectangular zones being produced from a centrally located vertical well.
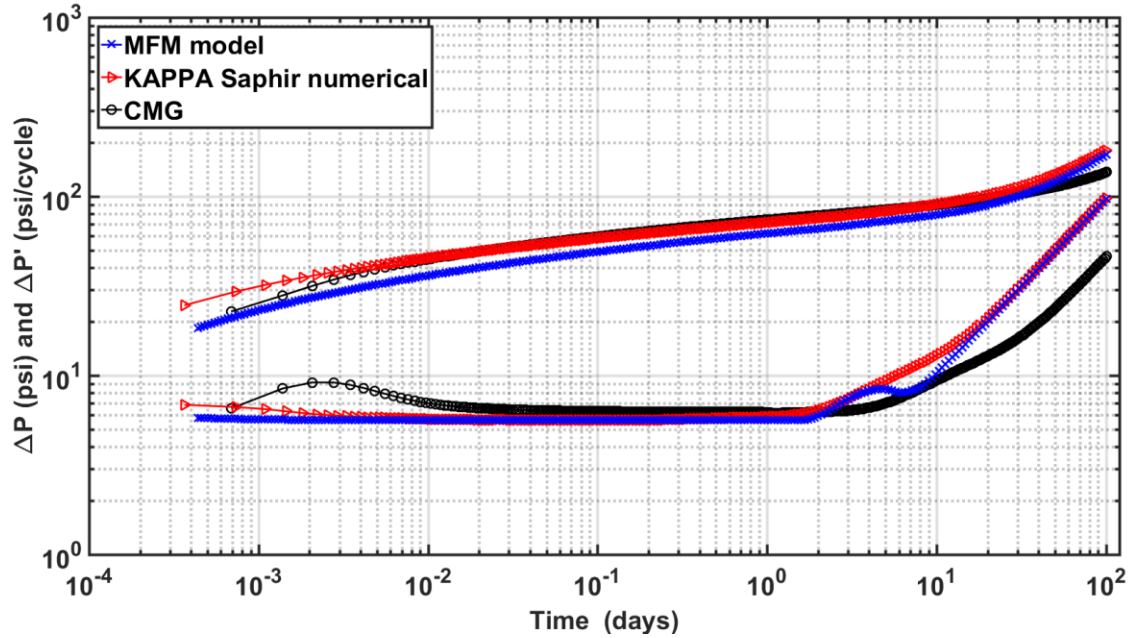
Figure 0.12: Diagnostic plot of pressure change and Bourdet-type pressure derivative responses of a vertical well in a bounded rectangular reservoir, shown in Figure 4.11, computed using MFM method, KAPPA Saphir numerical simulation, and CMG.

4.6 Conclusions

We applied improved MFM algorithm to highly heterogeneous reservoirs with high-contrast diffusivities. Our method is successfully utilized in the reservoirs with impermeable zones or relatively low-permeability zones. The algorithm is validated against KAPPA Rubis and CMG numerical solutions for generating pressure transient responses for wells located in reservoirs with high-contrast permeability distribution.

CHAPTER 5: MULTISTENCILS FAST MARCHING IN THE PRESENCE OF INFINITELY CONDUCTIVE FRACTURE

5.1 Review of Literature Survey for Fractured Network

Simulation techniques for naturally fractured reservoir (NFR) have drawn keen attention over the last decade. Accuracy of model predictions are challenged in zones of high-contrast diffusivity, thin-zones of high conductivity, and complex fracture networks (Moinfar et al., 2014). Discrete fracture network (DFN) modeling is commonly used to incorporate physically-consistent fracture geometry and topology (McClure et al., 2013; Delorme et al., 2013). In this modeling strategy, fracture is defined as an explicitly independent element in the fracture network. DFMs provide more-realistic representations of NFRs than dual-continuum models. The physical properties, such as storage, transmissibility, and the geometrical properties including the fracture position and magnitude, are statistically assigned to reservoir matrix with the information obtained from the laboratory studies and geological mapping (Shahid et al., 2016).

The modeling techniques in DFN is classified roughly into two types. The first one is changing grid size, shape, or coordinates in accordance with fracture geometry, similar to adaptive mesh grid, unstructured grid or local grid refinement method (Cipolla et al., 2011; Sun et al., 2015). The second methodology evaluates the fracture using fixed grids with embedded discrete fracture model or upscaled permeability method (Kang et al., 2013; HosseiniMehr, S. M., 2016). Local grid refinement is one of the most popular methods to simulate the fractures as a collection of smaller-sized grids. Nevertheless, this approach is computationally intensive for complex fracture geometry. Recent researches have been conducted to introduce unstructured grid system in fracture modeling instead

of Cartesian grid or corner point grid (Sun and Schechter, 2015; Yang et al., 2017). However, the computational cost problem remains when it is applied into the simulation of highly complex unconventional reservoirs. Despite the limitations, the unstructured grid is generally accepted as it ensures more accurate and elaborate modeling than local grid refinement. It is widely agreed that embedded discrete model is the most computationally efficient method (Chai et al., 2016).

In this chapter, we combine the discrete embedded fracture model with fast marching method to apply the proposed MFM method in complex NFR. This facilitates an accurate consideration of fracture influence on diffusive time of flight (DFT) calculations for accurate simulation of drainage volume and pressure derivative responses.

5.2 Methodology

The following sections introduces the improved MFM method capable of modeling natural fractures as discrete embedded fractures in the reservoir model. A novel Virtual Fracture Matrix (VFM) is developed and implemented in the earlier version of MFM method to consider the effect of the fractures on DTF calculations. The adopted methodology facilitates fracture modeling without local or adaptive grid refinement.

5.2.1 Concept of Embedded Fracture MFM

As mentioned earlier, the main aim of this chapter is to introduce a novel method for fracture treatments while keeping the computational cost within acceptable limits. For this purpose, this embedded fracture MFM method (EFMFM) is successfully used for evaluation of the effect of the fracture on diffusivity time of flight. FM method is a numerical technique that determines DTF from the nodes on the propagation front to all

50

the neighboring node, then selects the neighboring node with minimum DTF, and these two steps are iterated till all nodes in the reservoir are selected. Calculation of DTF between the selected node and neighboring node is based on the solution of Eikonal form of the high-frequency solution of the diffusivity equation that requires dividing the distance between the nodes by the diffusion speed of the grid connecting the node.

In Cartesian grid system, the DTF calculation is straightforward even with multistencils fast marching method because the distance between nodes is always constant. However, when a linear embedded fracture passes through multiple reservoir grids, as illustrated in **Figure 5.1a**, nodes on the linear fracture needs to be defined at the point of intersection of fracture and the reservoir grids; following that, the DTF from fracture node to neighboring nodes can be calculated using the distance between the nodes. Once the coordinates of fracture nodes and fracture properties are obtained, the diffusion time can be traced over the matrix and along the fracture simultaneously using EFMFM by following the procedure illustrated in **Figure 5.**

In the EFMFM method, front propagation in the reservoir nodes follows the algorithm for MFM method discussed in Chapter 4. When the front reaches the nodes close to the fracture nodes (black circles, **Figure 5.1b**), DTF is calculated to all the 7 neighboring unaccepted nodes points (gray circles, **Figure 5.1b**) to account for the presence of linear discrete fracture. Newly selected nodes include 3 fracture nodes and 4 reservoir nodes (gray circles, **Figure 5.1b**). Following that, the closest node, which in this case is the last fracture node, is selected as a next accepted node (black circles, **Figure 5.1b**) from where DTF will be calculated. In the next iteration, DTF is calculated to all the 8 neighboring unaccepted nodes points (gray circles, **Figure 5.1c**), such that

DTF calculation is performed for the two grids along the fracture. In case of conductive fracture, DTF along the fracture node is always faster compared to the DTF from fracture nodes to adjacent reservoir nodes; consequently, all fracture nodes are accepted as the front propagates (black circles, **Figure 5.1e**). Subsequently, DTF calculations are performed for propagation from fracture nodes to the adjacent reservoir nodes (gray circles, **Figure 5.1e**). After all the reservoir nodes adjacent to fracture nodes are estimated, (**Figure 5.1e**), the front propagation occurs based on the previously discussed MFM method. MFM algorithm is considerably changed to account for the extra diffusion paths along the fracture, as illustrated in **Figure 5.1c**, by implementing an additional matrix account for the propagation into, along, and out of the fracture nodes. This new matrix is referred as the Virtual Fracture Matrix.
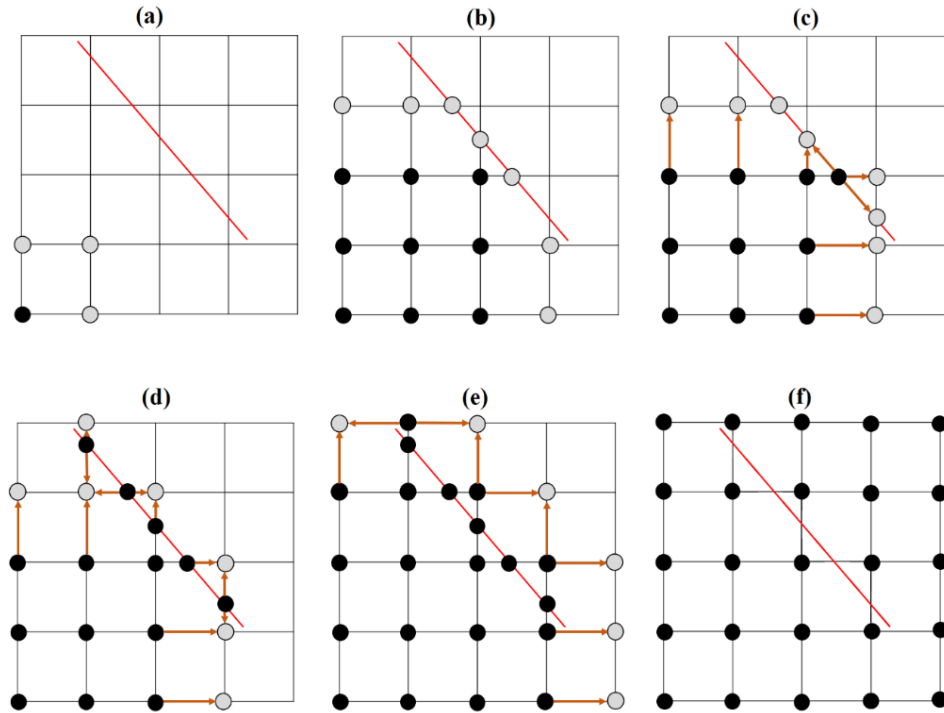
Figure 5.1: Schematic diagram of the algorithm for Embedded Fracture MFM for a reservoir containing a single linear infinite-conductivity fracture. Evolution of propagation front is shown chronologically from subplots a to f.

5.2.2 Virtual Fracture Matrix

Virtual Fracture Matrix (VFM) was created and implemented to model propagation of front from reservoir into fracture, along the fracture length, and out of the fracture back into the reservoir. An alternative computationally expensive approach is to increase the size of the matrix containing the DTF of all nodes and that containing the accepted and selected nodes by adding extra nodes identifying the fracture between adjacent reservoir nodes, which is similar to local grid refinement. Such an approach is challenging in naturally fractured reservoirs with complex fracture geometry and topology. We claim that the VFM approach that we adopt in our work is scalable for various fracture geometry and topology along with being computationally less expensive. In this approach, the fractures nodes and adjacent reservoir nodes along the horizontal and vertical grids are treated as a $3 \times n$ matrix, where n is the number of fracture nodes. Based on geometrical properties of a linear discrete fracture, namely location, slope, and length, first the adjacent reservoir nodes along the vertical and horizontal stencils are identified and indexed (**Figure 5.2a**). Following that, the fracture nodes are identified as points intersecting the stencils connecting the adjacent reservoir nodes (**Figure 5.2b**). All these aforementioned nodes are then placed into the $3 \times n$ VFM, such that three elements, two reservoir nodes and one fracture node, of each stencil are listed vertically in a way that share the common node in two adjacent columns (**Figure 5.2c**). Shared reservoir nodes are divided into two elements of the VFM, one on 1st row of a certain column and the other on the 3rd row of an adjacent column. As a result, first and third row of VFM represents reservoir nodes and its second row represents the fracture node.
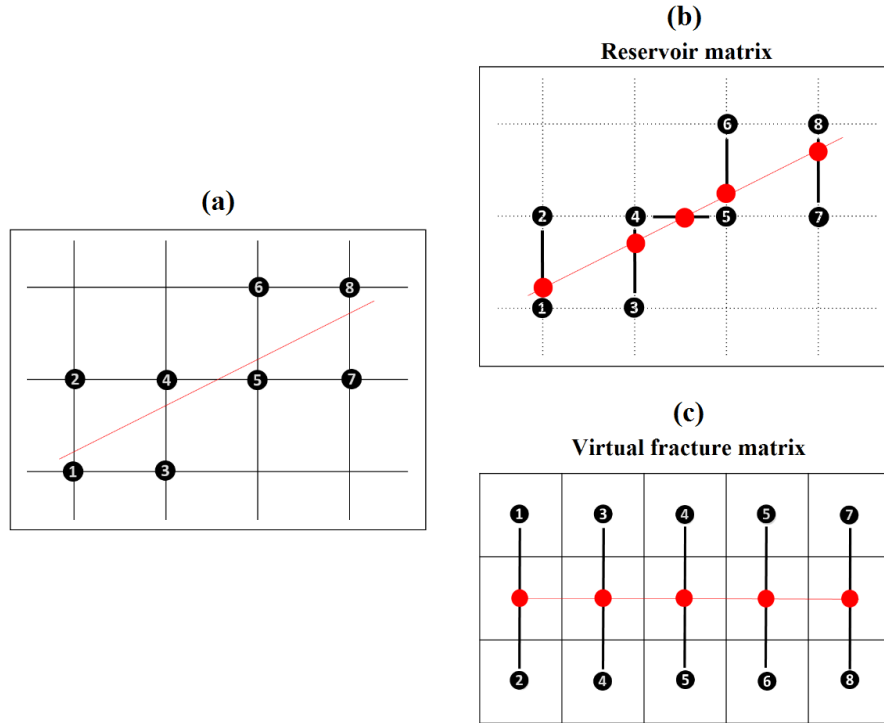
Figure 5.2: Schematic of generation of Virtual Fracture Matrix.

When a propagation front reaches an adjacent reservoir node, the propagation happens along the blue dotted lines of **Figure 5.3a** within the VFM. When the front reaches a fracture node, DTF is calculated in 3 directions towards the three unaccepted neighboring nodes. For fracture nodes, the propagation was modeled using FM algorithm. However, unlike conventional FM method, the DTF calculation for propagation from fracture nodes requires prior knowledge of the distance of the fracture node from its adjacent nodes and also the distinct diffusivity along the blue dotted lines because of the differences between fracture and reservoir properties. Accepted nodes are numbered sequentially beginning with 0 that progressively increases depending on the fracture propagation in the VFM, as shown in **Figure 5.3b**. The red star indicates the reservoir node that was reached by the propgation from the reservoir. The color scheme in **Figure 5.3b** indicates the time taken by the front to propagate through the fracture

system, such that darker color of a node indicates that the node was reached earlier than the nodes with lighter color. For the case shown in Figure 5.3 the propagation speed along the fracture is relatively similar to that in the adjoining node.

(a)

(b)
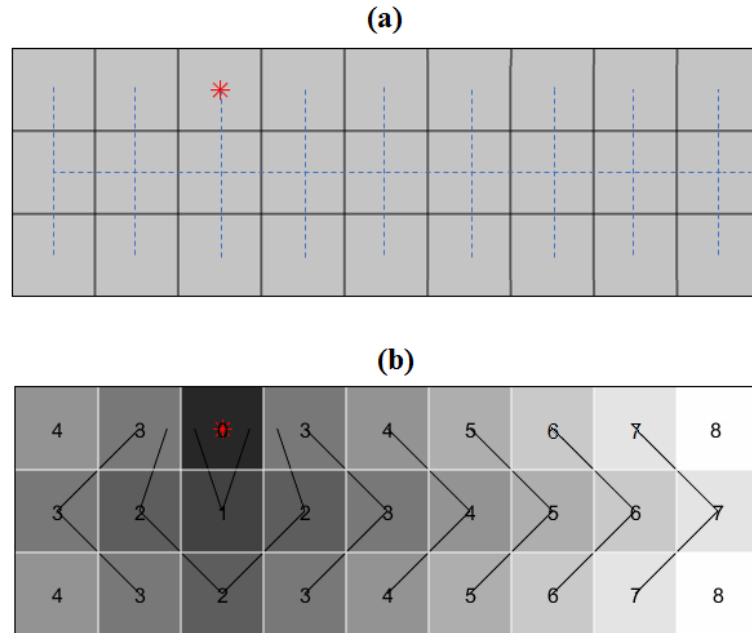
Figure 5.3: (a) Diffusion paths and (b) sequential propagation of front in the VFM.

Reliability of the VFM implementation needs to be tested with various fracture conductivities. In the numerical experiment presented in **Figure 5.4**, unlike the one shown in Figure 5.3, the distance between fracture nodes and reservoir nodes are considered for accurate modeling. A 10×10 reservoir model with a discrete linear fracture was used for this experiment. The propagation front propagates from well located at rightmost bottom corner and approaches the fracture from the reservoir node identified with blue square. For the first numerical experiment under the described scenario, reservoir permeability is assumed to be similar to fracture permeability. Therefore, differences in computed DTF between fracture and reservoir nodes shown in **Figure 5.4b** depends only on the distance between the nodes. For instance, the time taken

to reach the farthest corner of the fracture is similar to that required to reach its adjoining reservoir node. Also, there is a gentle gradation of color from darker to lighter in the VFM, which indicates relatively uniform propagation of front from one end to the other.
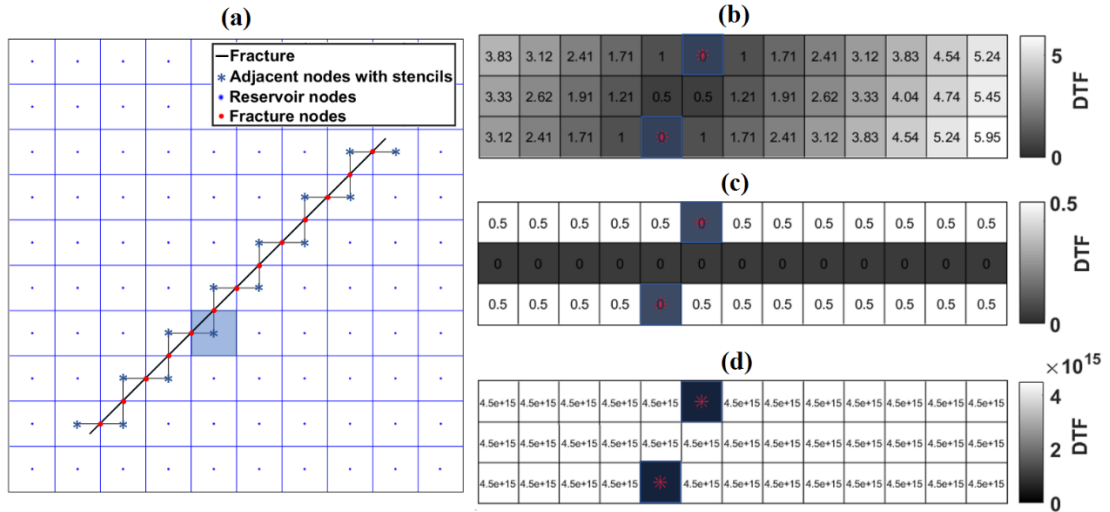
Figure 5.4: Computed DTF within VFM for (a) reservoir model with a fracture of (b) equal diffusivity, (c) infinite diffusivity, and (d) zero diffusivity. The reservoir is 10-ft by 10-ft and the DTF in VFM are computed after the propagation front reaches the blue shaded node.

For the infinite conductive fracture (**Figure 5.4c**), all elements in the second row identifying the fracture nodes have the same DTF as first accepted node (blue square). For the numerical experiment with non-conductive fracture, propagation will neither occur into the fracture nor across the fracture. Computed DTFs from fracture nodes to adjacent reservoir nodes are infinitely large (**Figure 5.4d**) that will force the propagation front to detour the fracture.

5.2.3 Algorithm of Embedded Fracture MFM with virtual fracture matrix.

Efficacy of the embedded fracture MFM method with the VFM is described using a 3×4 reservoir model containing an infinite-conductivity fracture (**Figure 5.5a**). We chose a small-sized reservoir model to quantitatively explain the workings of the

proposed FM method. Reservoir properties are assumed to be homogeneous. A producing well is located at the rightmost bottom corner. The reservoir nodes near the fracture are numbered and VFM is generated (**Figure 5.5a**) as described in the previous section. Propagation front reaches the reservoir node 3 (**Figure 5.5a**). For this reservoir node, two paths towards fracture nodes exist, which are also considered in VFM. DTF for the two paths are compared with rest of possible DTFs in the reservoir shown by arrow. The fracture node located vertically above the reservoir node 3 is accepted because of the lowest DTF required to reach to this fracture node (**Figure 5.5b**). Corresponding changes are recorded in the VFM. Subsequently, the DTF from the newly accepted fracture node to neighboring nodes and the reservoir node 3 to the previously unaccepted fracture node are computed in the VFM (**Figure 5.5b**).

The fracture being infinitely conductive, all the fracture nodes will be iteratively accepted to generate the front propagation pattern shown in **Figure 5.5c**. In the next iteration, DTF of all outward-bound propagation emerging from the fracture nodes are computed and compared with those for the reservoir nodes on the front. This results in sequential acceptance of reservoir nodes 2, 4, and 1, sequentially, based on distances between the nodes (**Figure 5.5d**). After all fracture nodes and adjacent reservoir nodes, all the surrounding reservoir nodes are determined, the EFMFM algorithm returns to MFM algorithm to finish the DTF calculations for the remaining reservoir nodes (**Figure 5.5d**). The flow chart, shown in **Figure 5.6**, summarizes the overall EFMFM algorithm.
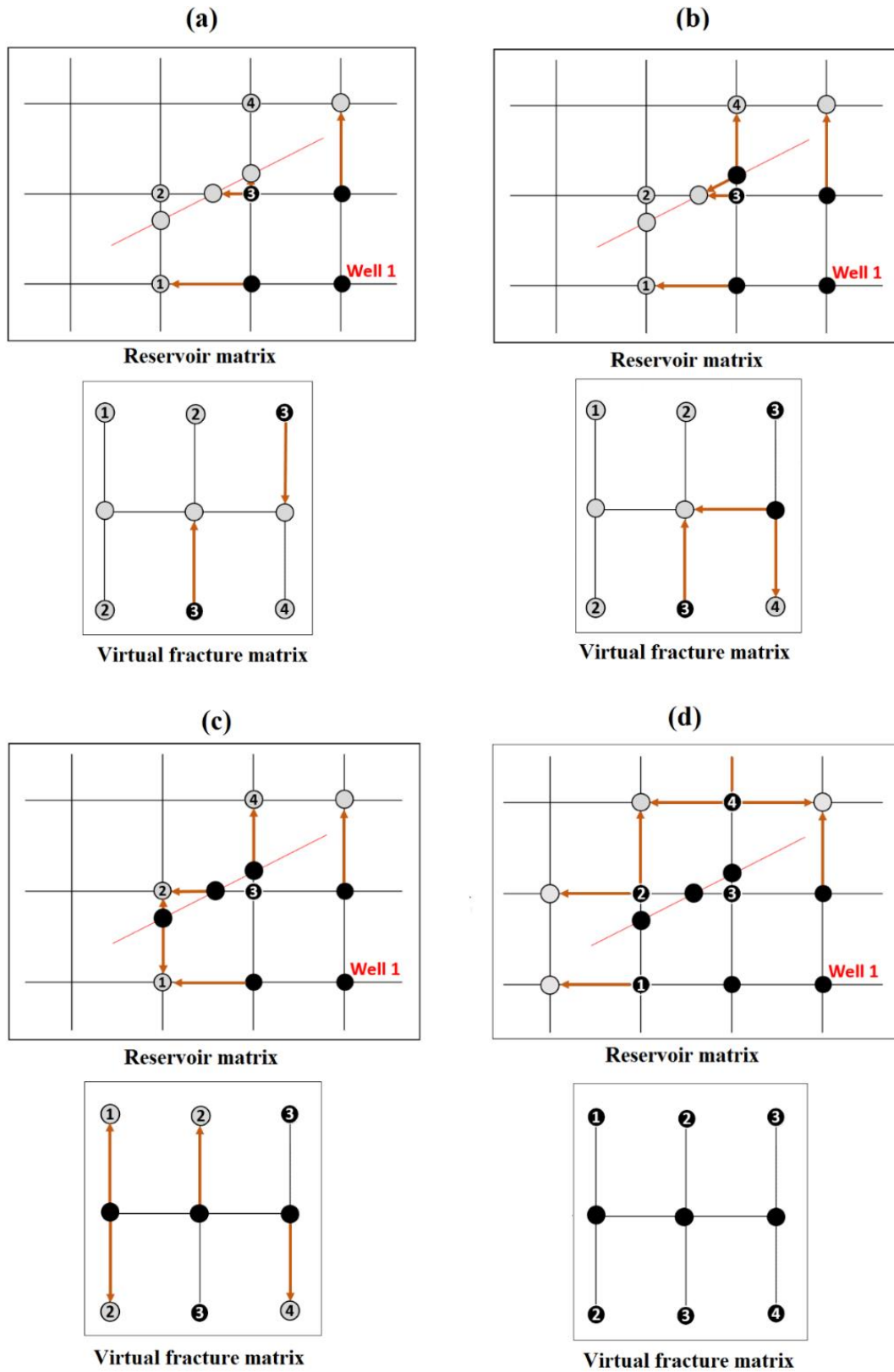
Figure 5.5: Schematic of the Embedded Fracture MFM with VFM algorithm applied to 3×4 reservoir containing single linear discrete fracture.

Figure 5.6: Flow chart for Embedded Fracture MFM with VFM.

5.3 Results and validations

5.3.1 Application of EFMFM on Reservoir with Single Linear Fracture

EFMFM algorithm here refers to the one that implements VFM. First, we demonstrate the simulations generated using EFMFM for reservoir models with larger number of nodes (**Figure 5.7**) compared to the case discussed in the previous section. A producing well is located in the rightmost bottom corner of the model. In this numerical

demonstration, we qualitatively validate the simulation results without trying to assess the numerical accuracy. **Figure 5.7a** presents the MFM model predictions in absence of fracture in the reservoir. A gradual variation in color from darker to lighter shade is observed indicating a relatively uniform propagation of the front. **Figure 5.7b** presents the EFMFM model predictions for reservoir containing single linear infinitely conductive fracture. The darker shade along the fracture indicates that pressure propagates faster along the fracture and then diffuses into the surrounding reservoir. Compared to the previous case, the presence of fracture results in arrival of pressure front at the leftmost top grid to be two times faster. It can be concluded that the EFMFM method qualitatively captures the effect of fracture on the front propagation without requiring additional local grid refinement. Notably, the darker-shaded elements in first and third rows of the VFM identify the reservoir nodes that are located closer to the fracture node compared to those that are of lighter shades.
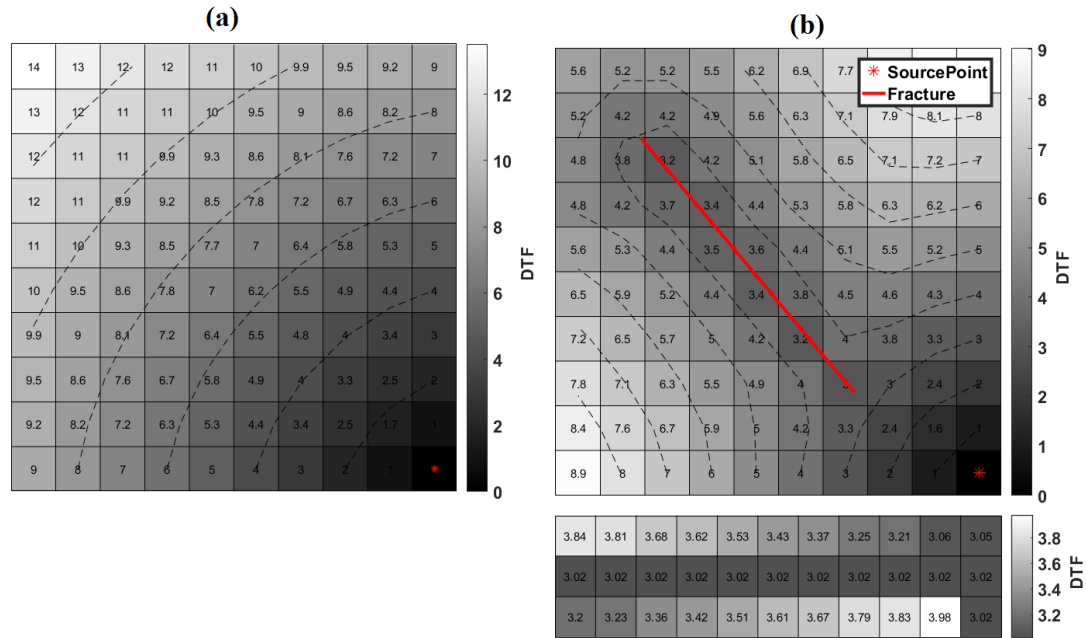
Figure 5.7: Diffusive time of flights predicted using (a) MFM algorithm for a reservoir without a fracture and those using (b) EFMFM algorithm for a reservoir with a single linear infintiely conductive fracture.

5.3.2 Comparison of Estimated DTF with Various Matrix Dimensions

The 10×0 reservoir model described in the previous section is not suitable to test numerical accuracy, which depends on the grid size. Numerical experiments presented in this section are performed for reservoir models ranging from 30×30 to 500×500 grids, such that each grid is 1-ft×1-ft. Simulation of pressure front propagation is investigated for various well locations and infinitely conductive fracture geometry, such as angle, length, and location. **Figure 5.8a** shows planar propagation above the fracture due to superposition and hemi-radial flow front the edges of the fracture. **Figure 5.8c** shows hemi-radial flow on the side geometrically opposite to the fracture and elliptical flow around the fracture.
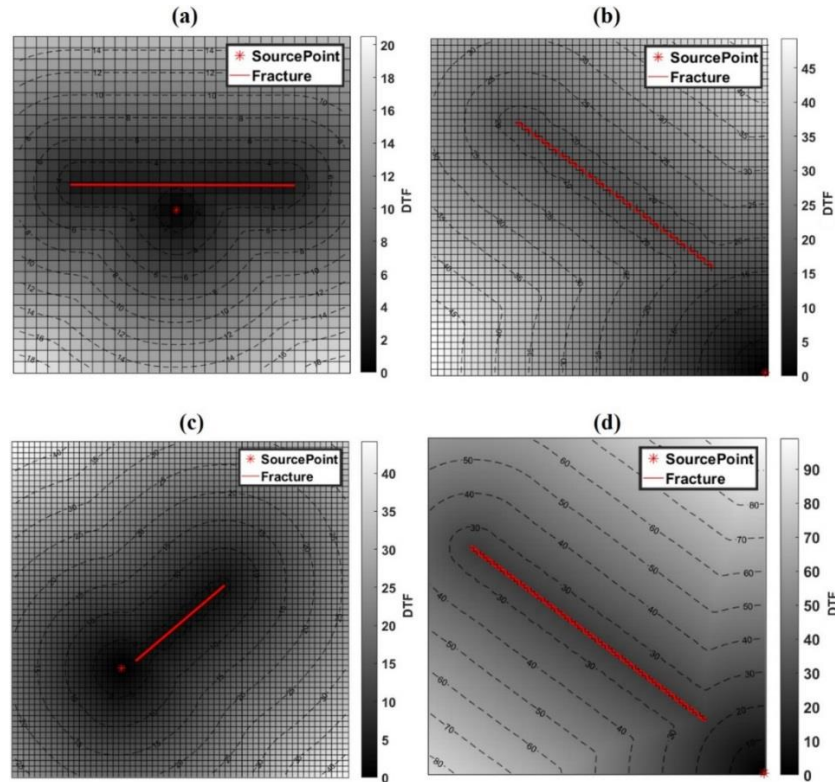
Figure 5.8: Simualtion of pressure front propagation generated using the EFMFM algorithm for various well locations and fracture geometries in reservoir models that are (a) 30-ft by 30-ft, (b) 50-ft by 50-ft, (c) 80-ft by 80-ft, and (d) 500-ft by 500-ft.

5.3.3 Comparison of Drainage Volume (MFM vs. EFMFM vs. KAPPA)

EFMFM method predictions are compared with KAPPA numerical simulations for circular bounded reservoirs of various size and fracture geometry. In this section, EFMFM predictions of drainage volume and pressure derivative response are validated. MFM method described in previous chapter is limited to blocky fractures, wherein grids of specific size (equal to those in the reservoir) are combined together to represent the fracture. Therefore, a slanted fracture cannot be accurately modeled as a collection of blocky fractures. In that case, accurate prediction of fracture effects requires extremely small grid sizes to describe the slanting fracture followed by local grid refinement.

EFMFM can efficiently handle slanted fracture without invoking small grids to define the fracture.

The drainage volume and pressure changes are simulated for circular bounded reservoir with single infinite conductivity fracture located close to a producing well. The 200-ft long fracture is located 28 ft away from the well at an angle of +45° with respect to *x*-axis. Fracture nodes are not collocated with reservoir nodes due to a 0.3-ft offset (**Figure 5.9a**). EFMFM simulation of this model is straightforward; however, MFM simulation requires a 45° rotation towards y-axis that allows the fracture to be modeled as collection of small-sized square grids (**Figure 5.9a**). KAPPA numerical simulator uses finite-difference and hexagonal grids to model the reservoir as shown in **Figure 5.9c**.

MFM and EFMFM predictions of drainage volume are in agreement (**Figure 5.10**). In **Figure 5.11**, the sudden drops in Bourdet-type derivative responses predicted by MFM and EFMFM models are detected around 0.07 days (4 hours) because the pressure front arrives at the edge of the fracture and then on the front rapidly propagates along the fracture. The boundary effect of unit slope in derivative response is predicted by MFM, EFMFM, and KAPPA simulations.

5.4 Conclusions

Here, we proposed a novel MFM-based method to analyze the effect of single linear infinitely conductive fracture on pressure front propagation. EFMFM method can simulate naturally fractured reservoirs with complex geometry and topology of fractures. EFMFM predictions of drainage volume and pressure derivative responses agree well with those generated using MFM method for simpler cases and KAPPA Rubis numerical simulations for complex cases. The strong point of EFMFM is that we can consider

heterogeneous permeability distribution and complex fracture geometry simultaneously to estimate time-varying drainage volume and pressure transient responses without adding numerous grid nodes or changing the grid format to account for the effects of linear fractures.

Table 5.1: Properties assumed for the case involving a vertical well centrally located in a circular no-flow circular bounded homogeneous reservoir with single infinite conductivity fracture, shown in Figure 5.9.

Reservoir property	
Dimension	*1,000 ft X 1,000 ft*
Grid size	*2 ft X 2 ft*
Initial pressure	*6000 psi*
Matrix permeability	*0.4 md*
Thickness	*10 ft*
Porosity	*0.1*
Radius of no-flow boundary	*500 ft*
Well/Fracture property	
Well radius	*0.25 ft*
Flowrate	*1 bbl/day*
Fracture total length	*200 ft*
Fluid property	
Viscosity	*0.4 cp*
Total compressibility	*$6.0 X 10^{-6} psi^{-1}$*
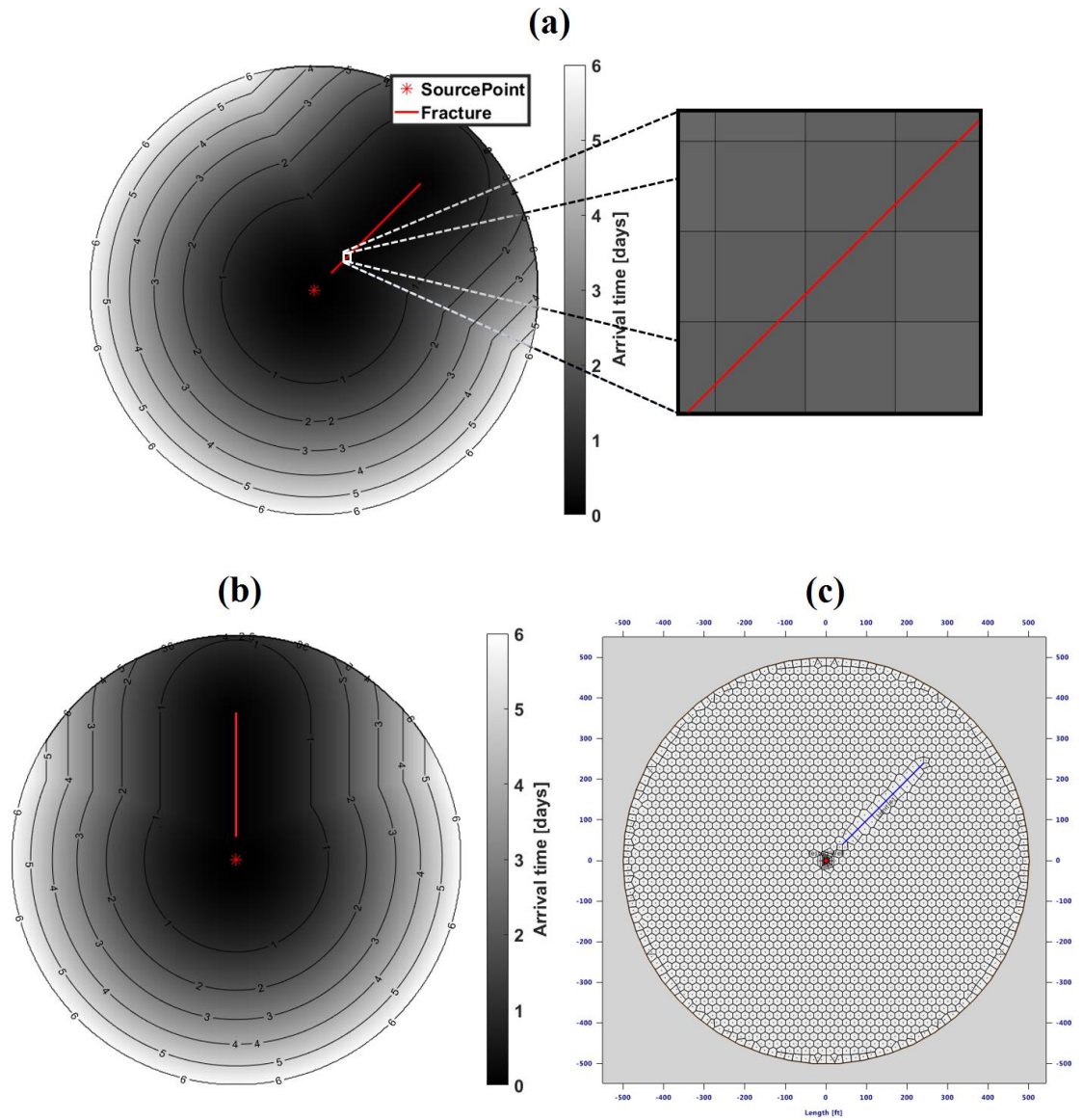
Figure 5.9: Travel-time computed using (a) EFMFM and (b) MFM method at *t* = 6 days and (c) grids generated in KAPPA Saphir numerical simulator for a circular bounded reservoir with a centrally located well and single linear infinitely-conductive fracture.

Figure 5.10: EFMFM and MFM predictions of time-varying drainage volumes for the reservoir scenario shown in Figures 5.9a and 5.9b, respectively.

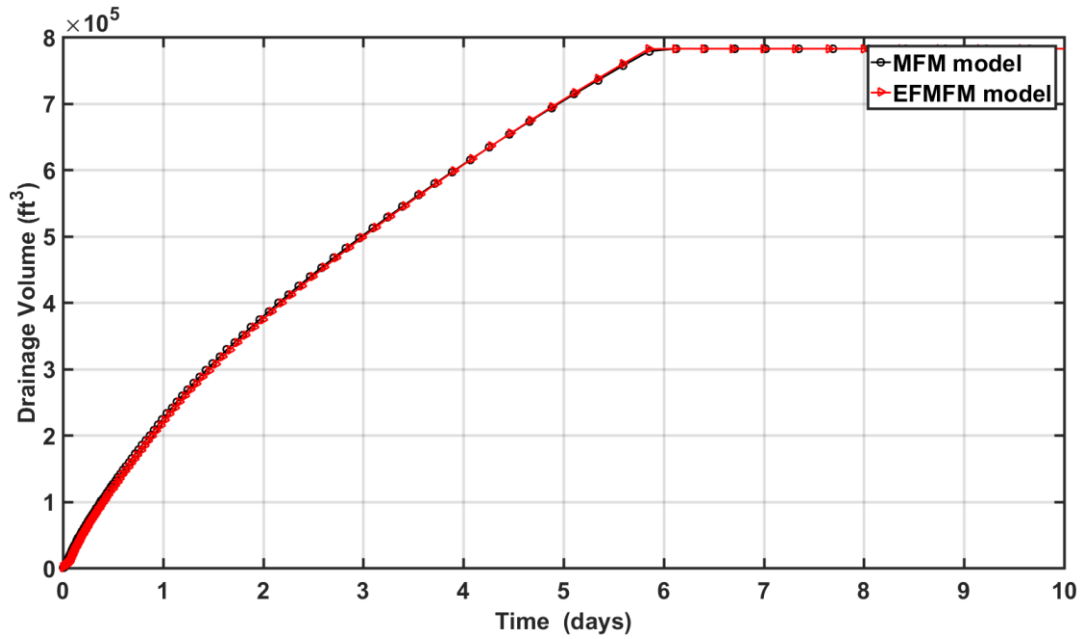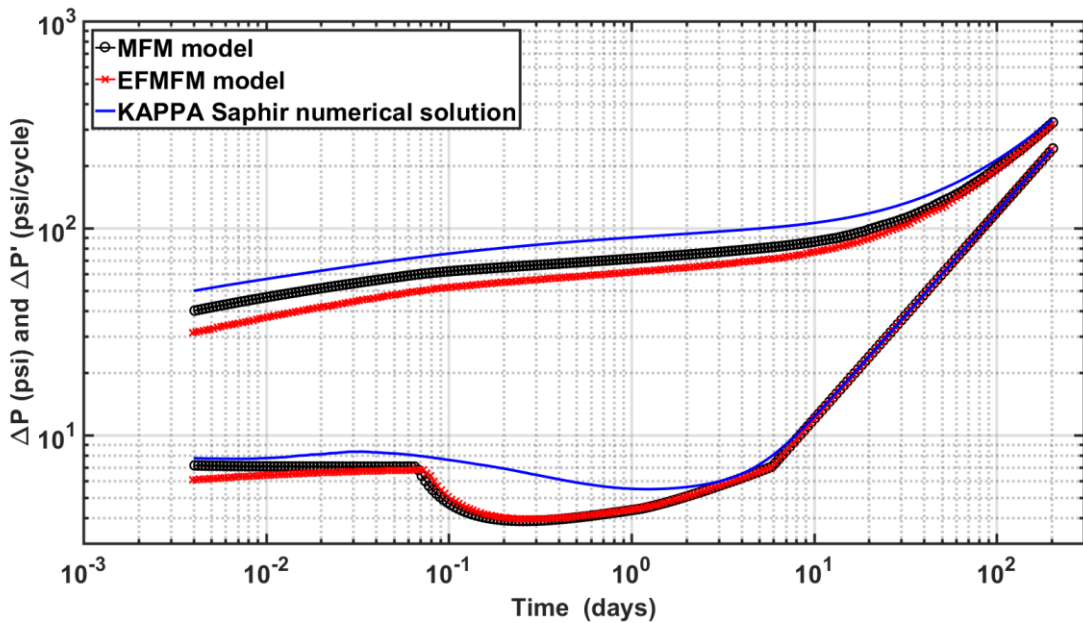**Figure 5.11: Pressure changes and Bourdet-type derivative responses of a vertical well centrally located in the bounded homogeneous reservoir, as described in Figure 5.9, computed using MFM method, EFMFM method, and KAPPA Saphir numerical model.**

CHAPTER 6: CONCLUSIONS AND RECOMMENDATIONS

6.1 Conclusions

Multistencils fast marching (MFM) method is developed to accurately model the two-dimensional pressure propagation in planar heterogeneous reservoir with heteromorphous no-flow reservoir boundary and natural fractures in vertical multiwell scenario at a low computational cost. Particularly, time-varying drainage volume and pressure derivative response can be modeled using this method to facilitate accurate pressure transient analysis. MFM method predictions were successfully validated and benchmarked against analytical and finite-difference numerical solutions for various reservoir scenarios. Predictions of the proposed MFM method are one order of magnitude more accurate then SFM predictions. Moreover, the MFM method has been improved to successfully perform simulation in high contrast permeability distribution and validated against commercial simulators. In MFM method, fracture was modeled as collection of square grids of a specific size and accordingly grids of the same width are generated for the entire reservoir, which immensely increases the computational time because the model of reservoir with fractures requires large number of small-sized square grids. To minimize this limitation in fracture modeling, embedded fracture multistencils fast marching (EFMFM) method is included in the algorithm to accommodate the effect of the fracture on diffusivity time of flight in the Cartesian grid system with low computational cost. The corresponding benefit of EFMFM is a large range of applications in reservoirs with high-contrast permeability distribution on Cartesian grids and linear fractures offset relative to the Cartesian grids.

6.2 Recommendations for Future Work

Following recommendations can improve current simulator to predict the drainage volume and pressure responses with more realistic reservoir scenarios accurately in a computationally efficient way. Firstly, skin effect near the wellbore and wellbore storage effect are not incorporated in the proposed algorithm. Our simulator does not have the capability to model the reservoirs with constant-pressure boundary and leaky boundary and with complex geometry of multiple intersecting fractures that have finite conductivity. Further research can be pursued to overcome these limitations. Once the EFMFM-based pressure front simulation accurately accounts for the complex geometry and topology of finite conductivity fracture, local grid refinements near the well, fractures, and high-contrast zones can be developed for improved pressure transient simulation. Finally, the simulator assumes that wells are fully penetrated with constant reservoir thickness and fractures have the same height as a reservoir thickness because it is 2-D simulator. Building a 3-D simulator with anisotropic diffusivity is also recommended for the future work.

NOMENCLATURE

α	Hydraulic diffusivity, ft^2/hr
A	Cross-sectional area, ft^2
$A_n(t)$	Pressure amplitude of the nth order in the time domain, $1/hr^{(n+2)/2}$
c_t	Compressibility, psi^{-1}
h	Reservoir thickness, ft
k	Permeability, md
P	Pressure, psi
$\bar{p}$	Average reservoir pressure, psi
$\tilde{p}$	Pressure in frequency domain, psi
p_i	Initial reservoir pressure, psi
Δp	Pressure drop, psi
P_{wf}	Bottomhole flowing pressure, psi
q	Flux, bbl/day
q_w	Flux at surface, bbl/day
r_w	Wellbore radius, ft
t	Arrival time of pressure front
$V(t)$	Time-dependent volume, ft^3
V_p	pore volume, ft^3
x_f	Fracture half length, ft
μ	Fluid viscosity, cp
ξ	Boltzmann variable, dimensionless
τ	Diffusive Time of Flight, $\sqrt{hr}$
ϕ	porosity, $fraction$
ω	Frequency of the asymptotic expansion, $1/S$

DTF	Diffusive Time of Flight
EFMFM	Embedded Fracture Multistencils Fast Marching
FM	Fast Marching
MFM	Multistencils Fast Marching
PTA	Pressure Transient Analysis
ROI	Radius of Investigation
SFM	Singlestencil Fast Marching
VFM	Virtual Fracture Matrix

REFERENCES

Capozzoli, A., Curcio, C., Liseno, A et al. 2014. Two-dimensional fast marching for geometrical optics. Optics Express 22:22, 26680 http://library.seg.org/doi/abs/10.1190/1.1468621

Chai, Z., Yan, B., and Killough, J. E. 2016. Dynamic Embedded Discrete Fracture Multi-Continuum Model for the Simulation of Fractured Shale Reservoirs. presented at International Petroleum Technology Conference held in Bangkok, Thailand, 14-16 November. IPTC-18887-MS. https://doi.org/10.2523/IPTC-18887-MS

Cipolla, C. L., Fitzpatrick, T., Williams, M. J. et al. 2011. Seismic-to-Simulation for Unconventional Reservoir Development. Presented at the SPE Reservoir Characterization and Simulation Conference and Exhibition, Abu Dhabi, 9–11 October. SPE- 46876-MS. http://dx.doi.org/10.2118/ 146876-MS.

Datta-Gupta, A., Xie, J., Gupta, N. et al. 2011. Radius of Investigation and Its Generalization to Unconventional Reservoirs. *J Pet Technol*, 63(7): 52–55.

Delorme, M., Daniel, J M., Kada-Kloucha, C et al. 2013. An efficient model to simulate reservoir stimulation and induced microseismic events on 3D discrete fracture network for unconventional reservoirs. presented Unconventional Resources Technology Conference, Denver, Colorado, 12-14 August 2013: pp. 1433-1442. URTeC 1578312. http://dx.doi.org/10.1190/urtec2013-146

Dey, B K., Ayers, P W., 2009. Computing the chemical reaction path with a ray-based fast marching technique for solving the Hamilton-Jacobi equation in a general coordinate system. *J. Mathematical Chemistry* 45:4, 981-1003. http://library.seg.org/doi/abs/10.1190/1.1468621

Dirami, A., Hammouche, K., Diaf, M, et al., 2012. Fast multilevel thresholding for image segmentation through a multiphase level set method. *J. Signal Processing*. 93:1, 139–153. https://doi.org/10.1016/j.sigpro.2012.07.010

Fatemi, E., B. Engquist, and S. Osher. 1995. Numerical solution of the high frequency asymptotic expansion for the scalar wave equation, *J. Comput. Phys*., 120, 145-155.

Gupta, N. (2012). A novel approach for the rapid estimation of drainage volume, pressure and well rates (Master Thesis, Texas A&M University).

Hassouna, M.S. and Farag, A. 2007. Multi-Stencils Fast Marching Methods: A Highly Accurate Solution to the Eikonal Equation on Cartesian Domains. IEEE Trans. Pattern Anal. 29 (9): 1563–1574.http:// dx.doi.org/10.1109/TPAMI.2007.1154.

HosseiniMehr, S. M. (2016) Multilevel Multiscale Method for Embedded Discrete Fracture Modeling Approach (F-MLMS) (Master Thesis, Delft University of Technology)

Janson, L., Schmerling E., Clark A. et al., 2015. Fast marching tree: A fast marching sampling-based method for optimal motion planning in many dimensions. *The Journal of Robotics Research.* 34:7, 883–921. DOI: 10.1177/0278364915577958

Kang, S., Datta-Gupta, A., Lee, W.J, 2013. Impact of natural fractures in drainage volume calculations and optimal well placement in tight gas reservoirs. *Journal of Petroleum Science and Engineering.* 109 206–216 https://doi.org/ 10.1016 /j.petrol.2013.08.024

Kim, J.U., Datta-Gupta, A., Brower, R. et al. 2009. Calibration of High-Resolution Reservoir Models Using Transient Pressure Data. Presented at the SPE Annual Technical Conference and Exhibition, New Orleans, Louisiana, 4–7 October. SPE-124834-MS. http://dx.doi.org/ 10.2118/124834-MS.

King, M. J., Wang. Z., Datta-Gupta. 2016. Asymptotic Solutions of the Diffusivity Equation and Their Applications. Presented at the SPE Europec featured at 78th EAGE Conference and Exhibition, Vienna, Austria, 30 May −2 June. SPE-180149-MS http:// dx.doi.org/10.2118/180149-MS

Lee, W.J. 1982. Well Testing. Richardson, Texas: Society of Petroleum Engineers.

Liu, Y., Bucknall, R., Zhang, X., 2017. The Fast Marching Method based Intelligent Navigation of an Unmanned Surface Vehicle. *J of Ocean Engineering.* https://doi.org/10.1016/j.oceaneng.2017.07.021

McClure, M.W., and Horne, R.N. 2013. Discrete Fracture Network Modeling of Hydraulic Stimulation Coupling Flow and Geomechanics, SpringerBriefs in Earth Sciences. http://dx.doi.org/10.1007/978-3-319-00383-2

Moinfar, A., Varavei, A., Sepehrnoori, Kamy et al., 2014. Development of an Efficient Embedded Discrete Fracture Model for 3D Compositional Reservoir Simulation in Fractured Reservoirs. Presented at the SPE Improved Oil Recovery Symposium, Tulsa, 14–18 April 2012. SPE-154246-MS. https://doi.org/10.2118/154246-MS

Rawlinson, N., Sambridge, M. 2004. Multiple reflection and transmission phases in complex layered media using a multistage fast marching method. *J of Geophysics,* 69:5, 1338-1350. http://library.seg.org/doi/abs/10.1190/1.1468621

Sethian, J. A. 1996. A Fast Marching Level Set Method for Monotonically Advancing Fronts. Proc. Natl. Acad. Sci. USA 93 (4): 1591–1595. http://dx.doi.org/ 10.1073/pnas.93.4.1591.

Shahid, A.S.A., Fokker, P.A., Rocca1, V. 2016. A Review of Numerical Simulation Strategies for Hydraulic Fracturing, Natural Fracture Reactivation and Induced Microseismicity Prediction. *The Open Petroleum Engineering Journal.,* vol. 9, pp. 72-91, DOI: 10.2174/1874834101609010072

Sun, J. and Schechter, D. 2015. Optimization-Based Unstructured Meshing Algorithms for Simulation of Hydraulically and Naturally Fractured Reservoirs with Variable Distribution of Fracture Aperture, Spacing, Length and Strike. SPE Res Eval & Eng 18 (4): 463–480. SPE-170703-PA. http://dx.doi.org/10.2118/170703-PA.

Sun, J., Schechter, D., Huang C. 2016. Grid-sensitivity analysis and comparison between unstructured perpendicular bisector and structured tartan/local-grid-refinement grids for hydraulically fractured horizontal wells in eagle ford formation with complicated natural fractures. *SPE J*. https://doi.org/10.2118/177480-PA

Vasco, D., Keers, H., and Karasaki, K. 2000. Estimation of Reservoir Properties Using Transient Pressure Data: An Asymptotic Approach. Water Resources Res. 36 (12): 3447–3465.

Xie, J. (2012). Applications of level set and fast marching methods in reservoir characterization (Master Thesis, Texas A&M University).

Xie, J., Gupta, N., King, M. J. et al. 2015. Depth of Investigation and Depletion Behavior in Unconventional Reservoirs Using Fast Marching Methods. *SPE J.* 20 (4): 831–841. SPE-154532-PA. http:// dx.doi.org/10.2118/154532-PA.

Yang, C., King, M J., and Datta-Gupta, A. 2017. Rapid Simulation of Naturally Fractured Unconventional Reservoirs with Unstructured Grids Using the Fast Marching Method presented at SPE Reservoir Simulation Conference held in Montgomery, TX, USA, 20–22 February. SPE-182612-MS. https://doi.org/10.2118/182612-MS

Zhang, Y., Yang, C., King, M. et al. 2013. Fast-Marching Methods for Complex Grids and Anisotropic Permeabilities: Application to Unconventional Reservoirs. Presented at the SPE Reservoir Simulation Symposium, The Woodlands, Texas, 18–20 February. SPE-163637-MS. http://dx.doi.org/10.2118/163637-MS.